Draft version September 6, 2024
Typeset using LATEX **twocolumn** style in AASTeX631

The James Webb Space Telescope Absolute Flux Calibration. II. Mid-Infrared Instrument Imaging and Coronagraphy

Karl D. Gordon ,[1,2] G. C. Sloan ,[1,3] Macarena Garcia Marin ,[1] Mattia Libralato ,[4,5] George Rieke ,[6]
Jonathan A. Aguilar ,[1] Ralph Bohlin ,[1] Misty Cracraft ,[1] Marjorie Decleir ,[7,*] Andras Gaspar ,[6]
David R. Law ,[1] Alberto Noriega-Crespo ,[1] and Michael Regan [1]

[1] *Space Telescope Science Institute, 3700 San Martin Drive, Baltimore, MD, 21218, USA*
[2] *Sterrenkundig Observatorium, Universiteit Gent, Gent, Belgium*
[3] *Department of Physics and Astronomy, University of North Carolina, Chapel Hill, NC 27599-3255, USA*
[4] *AURA for the European Space Agency (ESA), Space Telescope Science Institute, 3700 San Martin Drive, Baltimore, MD 21218, USA*
[5] *INAF, Osservatorio Astronomico di Padova, Vicolo dell'Osservatorio 5, Padova, I-35122, Italy*
[6] *Steward Observatory, University of Arizona, Tucson, AZ 85721, USA*
[7] *European Space Agency (ESA), ESA Office, Space Telescope Science Institute, 3700 San Martin Drive, Baltimore, MD 21218, USA*

ABSTRACT

The absolute flux calibration of the Mid-Infrared Instrument Imaging and Coronagraphy is based on observations of multiple stars taken during the first 2.5 years of JWST operations. The observations were designed to ensure that the flux calibration is valid for a range of flux densities, different subarrays, and different types of stars. The flux calibration was measured by combining observed aperture photometry corrected to infinite aperture with predictions based on previous observations and models of stellar atmospheres. A subset of these observations were combined with model point-spread-functions to measure the corrections to infinite aperture. Variations in the calibration factor with time, flux density, background level, type of star, subarray, integration time, rate, and well depth were investigated, and the only significant variations were with time and subarray. Observations of the same star taken approximately every month revealed a modest time-dependent response loss seen mainly at the longest wavelengths. This loss is well characterized by a decaying exponential with a time constant of ∼200 days. After correcting for the response loss, the band-dependent scatter around the corrected average (aka repeatability) was found to range from 0.1 to 1.2%. Signals in observations taken with different subarrays can be lower by up to 3.4% compared to FULL frame. After correcting for the time and subarray dependencies, the scatter in the calibration factors measured for individual stars ranges from 1 to 4% depending on the band. The formal uncertainties on the flux calibration averaged for all observations are 0.3 to 1.0%, with longer-wavelength bands generally having larger uncertainties.

Keywords: calibration

1. INTRODUCTION

Absolute calibration of astronomical observations is essential to many astrophysical investigations. A holistic approach is taken to calibrate all the James Webb Space Telescope (JWST) (JWST, Gardner et al. 2023) instruments consistently. At the same time, accurate calibration requires extending infrared calibration sequences to much fainter levels than has been the case previously before JWST (Gordon et al. 2022). This paper describes the steps to calibrate the Mid-Infrared Instrument (MIRI, Rieke et al. 2015; Wright et al. 2023); it is one of a series of papers covering all the JWST instruments.

MIRI on the James Webb Space Telescope (JWST, Gardner et al. 2023) provides imaging, coronagraphic, and spectroscopic observations in the mid-infrared from 5 to 28.8 μm. The absolute flux calibration of MIRI is based on observations of stars with well-modeled spectral energy distributions that have been taken as part of the overall JWST absolute flux-calibration program (Gordon et al. 2022). As for all the JWST instruments, the MIRI observations target stars of three different types and include multiple stars of each type. This coverage allows for both random and systematic uncertainties to be quantified. The combination of the cycle 1 and 2 JWST absolute flux-calibration program was constructed to enable accuracies of at least 5% and 10% for MIRI imaging and spectroscopy, respectively. Providing even higher accuracies is a goal of the program to enhance the JWST science. An explicit goal is to support science investigations using point and extended sources. See Gordon et al. (2022) for the details of the integrated JWST absolute flux calibration program for all JWST instruments.

---

[*] ESA Research Fellow

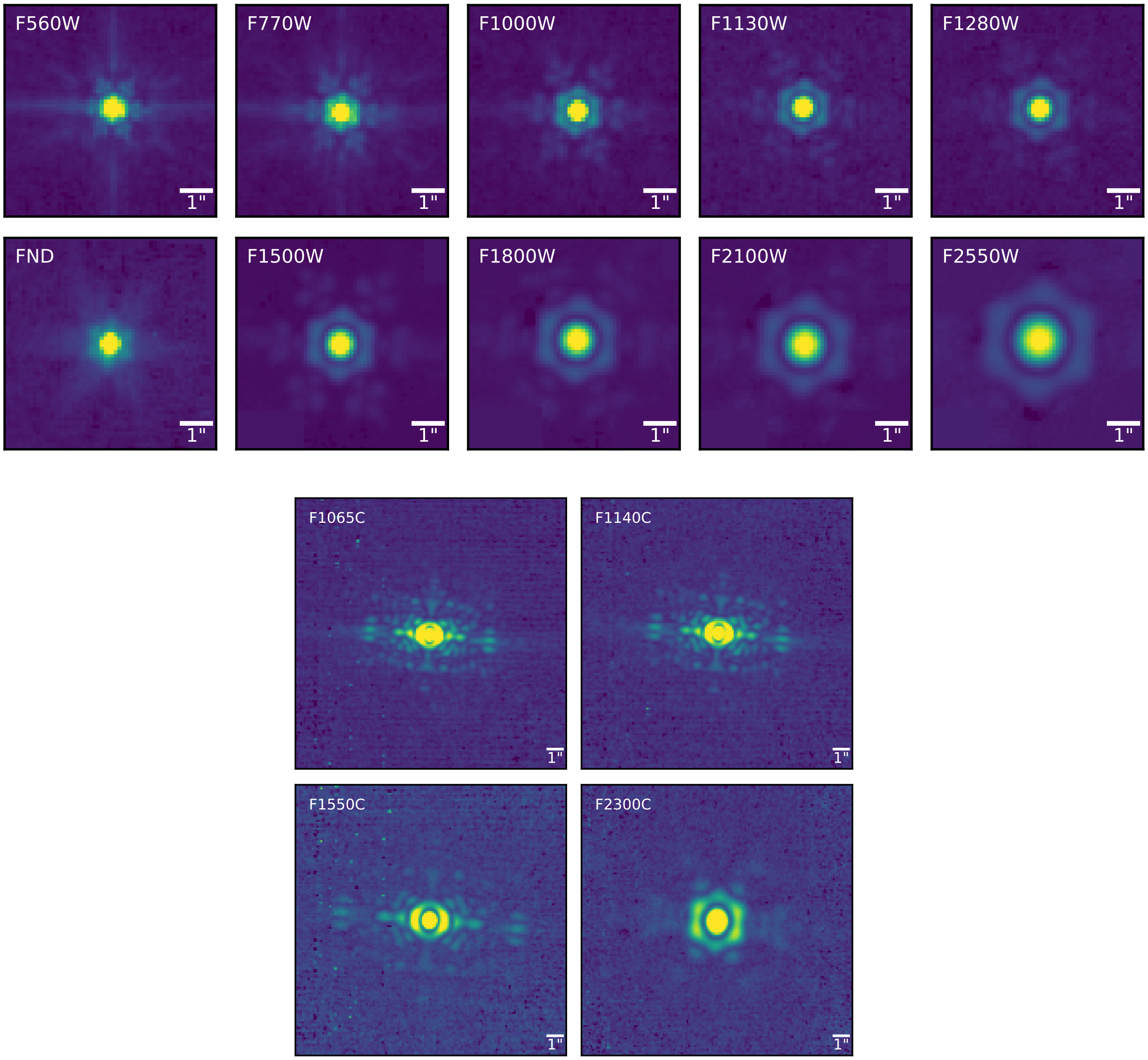

Figure 1. Example images for the imaging and coronagraphic filters to illustrate the data quality and general characteristics of MIRI point source observations. The targets include BD+60 1753 for the imaging bands from F560W to F1280W, δ UMi for the rest of the imaging bands, and HD 2811 for the coronagraphic bands. The image in the neutral density filter (FND) is smoother compared to the other imaging bands due to its wide bandpass. The coronagraphic observations were taken well away from the coronagraphic centers, and so these are the unocculted PSFs.

This paper presents the analysis of MIRI imaging and coronagraphic data taken over the first 2.5 years of JWST operations (i.e., Commissioning, cycle 1, and cycle 2). The overall goal of this analysis is to provide the flux calibration that converts the measured DN s^{-1} $pixel^{-1}$ values to physical MJy sr^{-1} surface brightness units for all the imaging and coronagraphic filters. The sources for which flux densities can be predicted at the accuracies required are generally limited to stars which are straightforward to model. A number of hot stars, A dwarfs, and Solar analogs with a range of flux densities were observed with all the MIRI imaging and coronagraphic filters. These observations were taken with different subarrays, different integration times, and were spread throughout the observing period. A critical part of this analysis is the derivation of aperture corrections to infinite apertures because the stellar model predictions are for the total flux densities. In addition, this correction explicitly allows the flux calibration to support both point and extended source science simultaneously by calibrating images to surface brightness units (Gordon et al. 2022).

Table 1. Hot Star Observations

Name	PID	Subarray	Bands
10 Lac	1524	FULL	FND
	4497	SUB64	F1000W, F1130W, F1280W, F1500W, F1800W, F2100W, F2550W
G 191-B2B	1537	FULL	F560W, F770W, F1000W, F1130W, F1280W, F1500W
GD 153	1537	FULL	F560W, F770W, F1000W
	4497	FULL	F560W, F770W, F1000W
GD 71	1537	FULL	F560W, F770W, F1000W
LAWD 87	4497	FULL	F560W, F770W, F1000W
WD 1057+719	4497	FULL	F560W, F770W
λ Lep	4497	SUB64	F1130W, F1280W, F1500W, F1800W, F2100W, F2550W
μ Col	4497	FULL	FND
		SUB64	F1000W, F1130W, F1280W, F1500W, F1800W, F2100W, F2550W

Table 2. Solar Analog Observations

Name	PID	Subarray	Bands
16 Cyg B	1538	FULL	FND
		SUB64	F1130W, F1280W, F1500W, F1800W, F2100W, F2550W
C26202	4498	FULL	F560W, F770W, F1000W
GSPC P177-D	1538	BRIGHTSKY	F560W, F770W, F1000W, F1130W, F1280W, F1500W, F1800W
GSPC P330-E	1538	BRIGHTSKY	F560W, F770W, F1000W, F1130W, F1280W, F1500W, F1800W
	4498	FULL	F560W, F770W, F1000W, F1130W, F1280W, F1500W, F1800W
		MASK1065	F1065C
		MASK1140	F1140C
HD 106252	1538	SUB64	F1000W, F1130W, F1280W, F1500W, F1800W, F2100W, F2550W
HD 1452331	4498	SUB64	F1000W, F1130W, F1280W, F1500W, F1800W, F2100W, F2550W
HD 167060	1538	FULL	FND
		MASK1065	F1065C
		MASK1140	F1140C
		MASK1550	F1550C
		MASKLYOT	F2300C
		SUB64	F770W, F1000W, F1130W, F1280W, F1500W, F1800W, F2100W, F2550W
HD 37962	1538	FULL	FND
		SUB64	F1000W, F1130W, F1280W, F1500W, F1800W, F2100W, F2550W
	4578	SUB64	F1280W, F1500W, F1800W, F2100W, F2550W
HR 6538	4498	FULL	FND
		SUB64	F1130W, F1280W, F1500W, F1800W, F2100W, F2550W
SNAP-2	4498	FULL	F560W, F770W, F1000W

§2 provides the details of the observations, the derivation of the apertures and aperture corrections, how the aperture photometry was performed, the flux densities predicted from models, and the zero-magnitude flux densities in the Sirius-Vega system. The calculation of the calibration factors is given in §3 along with the measurement of the temporal and subarray dependence of these factors. In addition, §3 illustrates the lack of any significant dependencies on flux density, background, type of star, central-pixel rate, central-pixel well depth, and integration time. §4 summarizes the results, and the appendix provides plots of the calibration factors from each star plotted versus all the dependencies investigated.

2. DATA

The main observations used for this work are those taken specifically for the absolute flux calibration in cycle 1 and 2 (PIDs: 1523, 1524, 1536, 1537, 1538, 1539, 4488, 4496, 4497, 4498, 4499, and 4578). A small amount of data taken in cycle 3 that was available at the time of this work are included (PID: 6607). These data were supplemented with observations taken during Commissioning that provide the preliminary absolute flux calibration (PID: 1027 and 1045). All of the targets were from the overall JWST absolute flux-calibration program and are highly vetted hot stars, A dwarfs, and Solar analog stars (Gordon et al. 2022). The exposure times were chosen to obtain data with signal-to-noise (S/N) ratios of 200 or better. Tables 1, 2, and 3, give the names of the stars, program identifications (PIDs), subarrays, and

Table 3. A Dwarf Observations

Name	PID	Subarray	Bands
2MASS J17430448+6655015	1027	FULL	F560W, F770W, F1000W, F1130W, F1280W, F1500W
	1536	FULL	F560W, F770W, F1000W, F1130W, F1280W, F1500W
2MASS J17571324+6703409	1533	BRIGHTSKY	F770W
		FULL	F770W
		SUB128	F770W
		SUB256	F770W
		SUB64	F770W
	1536	BRIGHTSKY	F560W
	4496	BRIGHTSKY	F560W, F770W, F1000W, F1130W, F1280W, F1500W, F1800W, F2100W
2MASS J18022716+6043356	1536	BRIGHTSKY	F560W, F770W, F1000W, F1130W, F1280W, F1500W, F1800W
	4488	BRIGHTSKY	F1280W
		FULL	F1280W
		SUB128	F1280W
		SUB256	F1280W
		SUB64	F1280W
BD+60 1753	1027	FULL	F1500W, F1800W, F2100W, F2550W
		SUB256	F560W, F770W, F1000W, F1500W
	1045	MASK1065	F1065C
		MASK1140	F1140C
		MASK1550	F1550C
		MASKLYOT	F2300C
	1536	SUB256	F560W, F770W, F1000W, F1130W, F1280W, F1500W, F1800W
	1539	SUB256	F770W
	4499	SUB256	F560W, F770W, F1000W, F1130W, F1280W, F1500W, F1800W, F2100W, F2550W
	6607	SUB256	F560W, F770W, F1000W, F1130W, F1280W, F1500W, F1800W, F2100W, F2550W
HD 101452	4496	BRIGHTSKY	F1500W, F1800W, F2100W, F2550W
HD 163466	1027	SUB64	F1000W, F1130W, F1280W, F1500W
	1536	FULL	FND
		SUB64	F1000W, F1130W, F1280W, F1500W, F1800W, F2100W, F2550W
	1539	FULL	FND
	6607	FULL	FND
HD 180609	1536	SUB128	F560W, F770W, F1000W, F1130W, F1280W, F1500W, F1800W, F2100W, F2550W
HD 2811	1523	SUB64	F770W, F1000W, F1130W, F1280W, F1500W, F1800W, F2100W, F2550W
	1536	FULL	FND
		MASK1065	F1065C
		MASK1140	F1140C
		MASK1550	F1550C
		MASKLYOT	F2300C
		SUB64	F770W, F1000W, F1130W, F1280W, F1500W, F1800W, F2100W, F2550W
	4496	BRIGHTSKY	F1500W, F1800W, F2100W, F2550W
		FULL	FND
		MASK1550	F1550C
		MASKLYOT	F2300C
HD 55677	4496	SUB256	F560W, F770W, F1000W, F1130W, F1280W, F1500W, F1800W, F2100W, F2550W
HR 5467	4496	FULL	FND
		SUB256	F1500W, F1800W, F2100W, F2550W
del UMi	1524	FULL	FND
	1536	FULL	FND
		MASK1065	F1065C
		MASK1140	F1140C
		MASK1550	F1550C
		MASKLYOT	F2300C
		SUB64	F1130W, F1500W, F1800W, F2100W, F2550W
	4578	SUB64	F1500W, F1800W, F2100W, F2550W

filters for the observations. A small number of observations from these programs suffered from various issues (e.g., failed guide-star acquisition, lost tracking, etc.), and these observations were not used in this work, nor are they listed in the tables.

The data were reduced using the JWST pipeline version 1.15.1 with the reference files specified by calibration reference data system pmap 1256, specifically using the CALWEBB_DETECTOR1, CALWEBB_IMAGE2, and CALWEBB_IMAGE3 stages. The standard steps for imaging data were performed except as described below. For the CALWEBB_DETECTOR1, the electromagnetic interference correction (emicorr) was not applied, and for the jump detection step (jump), the after-jump flagging and shower detection were skipped. For CALWEBB_IMAGE3, the outlier detection (outlier_detection), refinement of the relative astrometry (tweakreg), background matching (skymatch), and source catalog generation (source_catalog) steps were also skipped. In addition, the image combination step (resample) was run with a square kernel and the exposure time (exptime) weighting. These modifications to the standard reductions were made as well-exposed, high S/N observations with standard dithers do not benefit from some of the steps.

For the coronagraphic data, the data reduction was the same as imaging including the final mosaicking (e.g., CALWEBB_IMAGE3 instead of CALWEBB_CORON3). The motivation for using standard image mosaicking is that these observations were taken with the source placed well away from the center of the coronagraph and thus resemble imaging observations more than typical coronagraphic observations. To obtain reasonable parameters for the CALWEBB_IMAGE3 pipeline steps for coronagraphic data, the filter in the calibration exposures ("cal" files) was changed to the closest-in-wavelength imaging filter.

In addition to the standard processing to produce mosaics, we also generated mosaics with custom image-based background subtraction for each exposure before mosaicking. The custom background for each band was created by averaging the stack of all the exposures in an observation aligned in detector coordinates. Before obtaining this mean, the region within the full width at half maximum (FWHM) of the source was masked to ensure the mean background did not include any of the source signal. These background-subtracted images and mosaics are important in cases where the background is strong and/or has significant structure, which happens in all of the coronagraphic bands due to significant scattered light (Boccaletti et al. 2022). The F2550W imaging band is affected similarly.

Fig. 1 shows example mosaics created using the custom image-based background subtraction.

2.1. *Apertures and Corrections*

The photometric apertures and background annuli for measuring the flux of each star were set based on the point-spread-functions (PSFs) in each band. Specifically, radial profiles of encircled energy were used, with the aperture radius (r_a) set to include 70% of the flux and the background annulus set between the radii that include 80% and 85% of the flux (r_{b1} and r_{b2}). The background annulus includes contributions from the actual background and from the source itself due to the PSF. Thus, the aperture corrections necessarily depend on the background annulus parameters in addition to the object aperture radius. With these radii values, the aperture correction to infinite aperture can be computed as

$$A_{\rm cor} = \frac{1}{0.7 - S_{\rm bkg}\pi r_a^2} \tag{1}$$

where the background surface brightness per pixel due to the PSF wings is

$$S_{\rm bkg} = \frac{0.85 - 0.8}{\pi(r_{b2}^2 - r_{b1}^2)}. \tag{2}$$

The radial encircled energy profiles were computed using a combination of observed and model PSFs. It is not possible to create PSFs from observations alone as determining the background level far from the source is challenging given variations in the background due to residual detector and instrument effects, other astronomical sources, and measurement noise. Using a model for the PSF based on the optics of the telescope and instrument is possible, but the structure at small radii in the observations does not match the model well, especially at the shorter MIRI wavelengths. One known detector issue that may affect the core is the "brighter-fatter effect" (BFE; Argyriou et al. 2023). This effect arises when large differences in accumulated charge between neighboring pixels results in the diffusion of some charge to pixels with lower accumulated charge. §3.5 investigates the impact of BFE on the aperture photometry. The model PSF was created using WebbPSF v1.3.0 (Perrin et al. 2012, 2014) using the option that includes detector artifacts including the cruciform (Gáspár et al. 2021; Dicken et al. 2024).

Hence, the MIRI PSFs are generated by using the observed radial PSFs inside a given radius and the model PSF outside this radius. We did not use the existing effective PSFs (ePSFs) because they were not designed to measure the encircled energy due to smoothing and their normalization to unity area at a finite radius (Libralato et al. 2024). For the imaging filters, observations of BD+60 1753 were used for the observed PSF as it had multiple, high S/N observations with no visually obvious sources within 10″. For the FND filter, δ UMi was used. For the coronagraphic filters, observations of HD 2811, δ UMi, and 16 Cyg B were used. The observed radial PSFs are multiplicatively corrected to match the model PSF at a given radius. The radius where the PSFs transition between the observed and the model PSFs was determined based on visually inspecting the observed radial profiles and choosing the largest radius at each wavelength that did not show obvious extraneous structure (i.e., encircled energy decreasing with increasing radius). The radii used for all bands were approximately 40 pixels, which corresponds to $\sim$4.5″. It was not possible to determine a high-quality observed PSF for F2550W due to large variations in the background. Hence, the model PSF is adopted for all radii for this filter. This solution for F2550W is reasonable given that the difference between the model PSFs and observed PSFs decreases

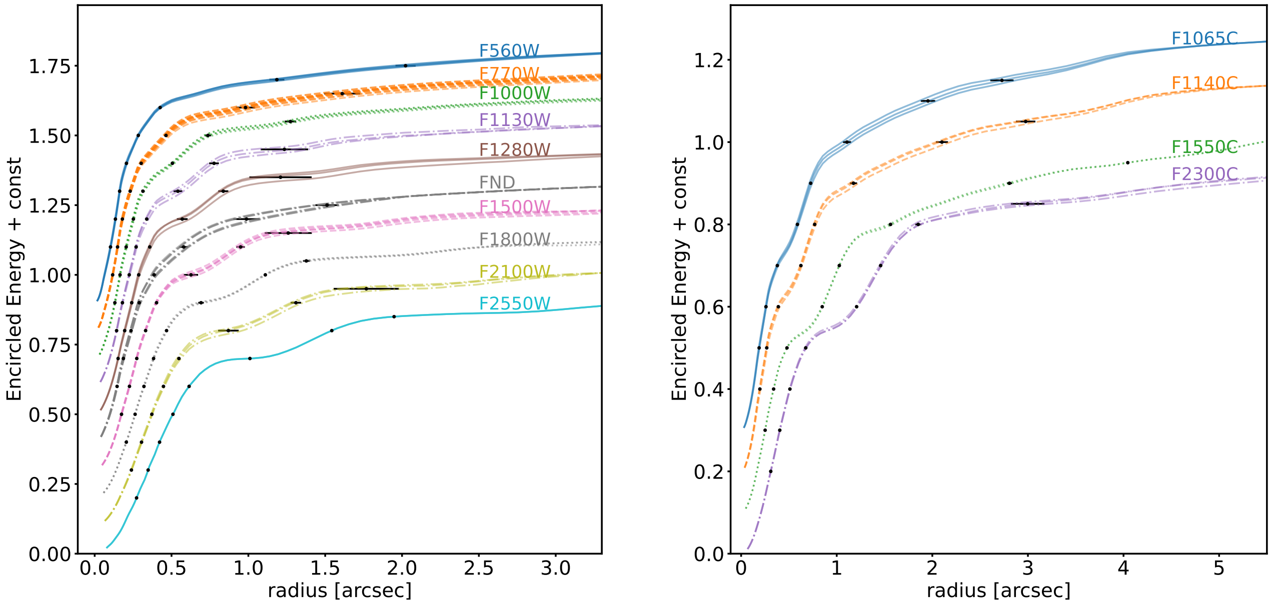

Figure 2. The radial encircled energies for the imaging (left) and coronagraphic (right) bands. Subsequent bands are offset by a factor of 0.1. Multiple radial encircled energies are plotted for each band using repeated observations except F2550W, which is based on the WebbPSF model at all radii. The black points give the radii for 0.2, 0.3, 0.4, 0.5, 0.6, 0.7, 0.8, and 0.85 encircled energies with their uncertainties as horizontal lines. The radii uncertainties are based on the scatter of the radii computed from independent observations. The coronagraphic profiles are broader than the imaging profiles, and the Lyot F2300C profile is narrower than expected given an extrapolation of the behavior of the three 4QPM coronagraphic profiles (F1065C, F1140C, and F1550C). This is due to the difference in type of coronagraph.

with wavelength and becomes quite small for F1800W and F2100W. Fig. 2 shows how the final encircled energies depend on wavelength for all of the bands. The increasing PSF width with wavelength is clearly seen along with the signature of the first and second Airy rings. The FND band shows smoother variation than other imaging bands because its wide bandpass washes out the Airy rings. The coronagraphic filters have larger widths than imaging bands with similar wavelengths due to the extra coronagraphic optical elements (Perrin et al. 2018; Boccaletti et al. 2015). The uncertainties are determined from the multiple observations in the same filter. The radii are larger than expected for the F560W and F770W filters compared to the behavior of the F1000W and longer filters due to the extra cruciform component that deflects light below 10 μm inside the detector material to larger radii.

To determine the absolute flux calibration, we use radii for 70% of the encircled energy with the sky annulus between the radii for 80 and 85% of the encircled energies. Table 4 gives the radii and aperture corrections for these choices for all of the bands. The uncertainties in radii are strongly influenced by the steepness of the encircled energy profile. For example, the r_{b2} uncertainties are often significantly larger than the r_{b1} as the 85% points on the encircled energy curves are much less steep than the 80% points. The reference file for the aperture correction in the JWST pipeline provides the aperture corrections for encircled energies between 0.1 and 0.8 using background annuli defined by 80 and 85 % of the encircled energies[1].

Table 4. Apertures and Corrections

Band	r_a (pix)	r_{b1} (pix)	r_{b2} (pix)	$A_{\rm cor}$
F560W	3.87 ± 0.06	10.78 ± 0.44	18.39 ± 0.59	1.671 ± 0.0002
F770W	4.22 ± 0.10	8.92 ± 0.57	14.64 ± 1.07	1.675 ± 0.0008
F1000W	4.60 ± 0.08	6.70 ± 0.19	11.58 ± 0.34	1.679 ± 0.0004
F1130W	4.92 ± 0.26	7.06 ± 0.29	11.22 ± 1.40	1.686 ± 0.0079
F1280W	5.18 ± 0.32	7.61 ± 0.30	10.99 ± 1.84	1.696 ± 0.0130
FND	5.27 ± 0.26	8.98 ± 0.78	13.74 ± 0.69	1.683 ± 0.0007
F1500W	5.69 ± 0.43	8.63 ± 0.26	11.45 ± 1.39	1.706 ± 0.0146
F1800W	6.29 ± 0.17	10.09 ± 0.04	12.52 ± 0.20	1.714 ± 0.0030
F2100W	7.91 ± 0.61	11.90 ± 0.31	16.07 ± 1.93	1.702 ± 0.0120
F2550W*	9.18 ± 0.00	14.03 ± 0.00	17.71 ± 0.00	1.705 ± 0.0000
F1065C	10.07 ± 0.39	17.77 ± 0.68	24.80 ± 1.11	1.687 ± 0.0015
F1140C	10.68 ± 0.35	19.10 ± 0.58	27.06 ± 0.92	1.685 ± 0.0009
F1550C	14.21 ± 0.16	25.52 ± 0.25	36.77 ± 0.05	1.684 ± 0.0005
F2300C	13.27 ± 0.08	16.84 ± 0.29	27.25 ± 1.59	1.705 ± 0.0060

* F2550W does not have measured uncertainties as the model PSF was used for all radii.

---

[1] https://jwst-crds.stsci.edu/

Table 5. Photometry

name	PID	srctype	filter	subarray	time	pixrate	pixwelldepth	inttime	iflux	ifluxunc	ibkg	flux	fluxunc	bkg
					MJD	DN s^{-1}	DN	s	DN s^{-1}	DN s^{-1}	DN s^{-1}	mJy	mJy	MJy sr^{-1}
16 Cyg B	1538	SolarAnalogs	F1130W	SUB64	59762.5	5.17e+04	4.40e+04	0.85	8.79e+05	1.07e+03	1.43e+02	4.14e+02	5.03e-01	1.61e+02
16 Cyg B	1538	SolarAnalogs	F1280W	SUB64	59762.5	9.02e+04	4.61e+04	0.51	1.80e+06	2.45e+03	4.08e+02	3.26e+02	4.43e-01	1.74e+02
16 Cyg B	1538	SolarAnalogs	F1500W	SUB64	59762.5	5.91e+04	4.02e+04	0.68	1.49e+06	4.31e+03	6.57e+02	2.39e+02	6.91e-01	2.46e+02
16 Cyg B	1538	SolarAnalogs	F1800W	SUB64	59762.5	2.55e+04	2.17e+04	0.85	7.98e+05	2.34e+03	5.01e+02	1.69e+02	4.95e-01	2.46e+02
16 Cyg B	1538	SolarAnalogs	F2100W	SUB64	59762.5	1.80e+04	1.54e+04	0.85	7.33e+05	1.11e+03	6.32e+02	1.28e+02	1.93e-01	2.59e+02
16 Cyg B	1538	SolarAnalogs	F2550W	SUB64	59762.5	5.23e+03	1.34e+04	2.55	2.47e+05	6.08e+02	1.11e+03	8.12e+01	2.00e-01	8.51e+02
2MASS J17430448+6655015	1027	ADwarfs	F560W	FULL	59737.6	6.68e+02	1.85e+04	27.75	4.76e+03	7.35e+00	3.19e+00	8.78e-01	1.36e-03	1.43e+00
2MASS J17430448+6655015	1027	ADwarfs	F560W	FULL	59724.4	3.91e+02	1.09e+04	27.75	3.38e+03	7.09e+00	3.43e+00	6.24e-01	1.31e-03	1.54e+00
2MASS J17430448+6655015	1536	ADwarfs	F560W	FULL	59763.0	5.92e+02	1.64e+04	27.75	4.71e+03	7.10e+00	3.28e+00	8.69e-01	1.31e-03	1.47e+00
2MASS J17430448+6655015	1027	ADwarfs	F560W	FULL	59727.9	6.52e+02	1.81e+04	27.75	4.78e+03	5.33e+00	3.23e+00	8.83e-01	9.84e-04	1.45e+00
2MASS J17430448+6655015	1027	ADwarfs	F770W	FULL	59727.9	5.64e+02	1.57e+04	27.75	4.69e+03	6.72e+00	1.86e+01	4.99e-01	7.15e-04	4.79e+00
2MASS J17430448+6655015	1536	ADwarfs	F770W	FULL	59763.0	5.18e+02	1.44e+04	27.75	4.67e+03	6.37e+00	1.70e+01	4.97e-01	6.78e-04	4.38e+00
2MASS J17430448+6655015	1027	ADwarfs	F770W	FULL	59737.6	5.18e+02	1.44e+04	27.75	4.66e+03	6.38e+00	1.75e+01	4.95e-01	6.78e-04	4.51e+00
2MASS J17430448+6655015	1536	ADwarfs	F1000W	FULL	59763.1	1.99e+02	5.53e+03	27.75	2.03e+03	4.58e+00	3.46e+01	2.92e-01	6.58e-04	1.20e+01
2MASS J17430448+6655015	1027	ADwarfs	F1000W	FULL	59737.6	2.01e+02	5.56e+03	27.75	2.05e+03	4.68e+00	3.56e+01	2.94e-01	6.72e-04	1.23e+01
2MASS J17430448+6655015	1027	ADwarfs	F1000W	FULL	59727.9	2.10e+02	5.84e+03	27.75	2.04e+03	4.77e+00	3.75e+01	2.92e-01	6.85e-04	1.30e+01
2MASS J17430448+6655015	1536	ADwarfs	F1130W	FULL	59763.1	4.84e+01	2.68e+03	55.50	5.03e+02	1.84e+00	1.56e+01	2.29e-01	8.39e-04	1.69e+01
2MASS J17430448+6655015	1027	ADwarfs	F1130W	FULL	59737.6	5.07e+01	2.81e+03	55.50	5.02e+02	2.06e+00	1.60e+01	2.29e-01	9.39e-04	1.73e+01
2MASS J17430448+6655015	1027	ADwarfs	F1130W	FULL	59727.9	5.13e+01	2.85e+03	55.50	5.00e+02	1.89e+00	1.67e+01	2.27e-01	8.61e-04	1.81e+01
2MASS J17430448+6655015	1536	ADwarfs	F1280W	FULL	59763.1	1.11e+02	4.91e+03	44.40	1.01e+03	4.34e+00	5.36e+01	1.76e-01	7.59e-04	2.21e+01
2MASS J17430448+6655015	1027	ADwarfs	F1280W	FULL	59727.9	1.14e+02	5.08e+03	44.40	1.02e+03	4.57e+00	5.68e+01	1.78e-01	7.95e-04	2.33e+01
2MASS J17430448+6655015	1027	ADwarfs	F1280W	FULL	59737.6	1.11e+02	4.94e+03	44.40	1.02e+03	4.37e+00	5.49e+01	1.77e-01	7.61e-04	2.25e+01
2MASS J17430448+6655015	1027	ADwarfs	F1500W	FULL	59737.6	1.44e+02	3.44e+04	238.90	8.47e+02	3.02e+00	1.09e+02	1.31e-01	4.67e-04	3.91e+01
2MASS J17430448+6655015	1027	ADwarfs	F1500W	FULL	59727.9	1.47e+02	3.51e+04	238.90	8.66e+02	2.60e+00	1.11e+02	1.34e-01	4.01e-04	3.99e+01
2MASS J17430448+6655015	1536	ADwarfs	F1500W	FULL	59763.1	1.44e+02	7.21e+03	49.95	8.44e+02	4.17e+00	1.08e+02	1.31e-01	6.46e-04	3.89e+01
G 191-B2B	1537	HotStars	F560W	FULL	59830.4	6.85e+02	1.90e+04	27.75	4.39e+03	6.49e+00	4.81e+00	8.11e-01	1.20e-03	2.16e+00
G 191-B2B	1537	HotStars	F770W	FULL	59830.4	5.33e+02	1.48e+04	27.75	4.30e+03	6.47e+00	3.10e+01	4.58e-01	6.88e-04	7.99e+00
G 191-B2B	1537	HotStars	F1000W	FULL	59830.4	2.07e+02	5.74e+03	27.75	1.91e+03	5.37e+00	5.72e+01	2.75e-01	7.75e-04	1.98e+01
G 191-B2B	1537	HotStars	F1130W	FULL	59830.4	5.73e+01	3.82e+03	66.60	4.72e+02	2.12e+00	2.59e+01	2.15e-01	9.65e-04	2.82e+01
G 191-B2B	1537	HotStars	F1280W	FULL	59830.4	1.36e+02	6.06e+03	44.40	9.71e+02	5.08e+00	8.14e+01	1.71e-01	8.95e-04	3.38e+01
G 191-B2B	1537	HotStars	F1500W	FULL	59830.4	1.77e+02	1.18e+04	66.60	8.29e+02	4.30e+00	1.42e+02	1.29e-01	6.70e-04	5.17e+01

NOTE—Table 5 is published in its entirety in the machine-readable format. A portion is shown here for guidance regarding its form and content.

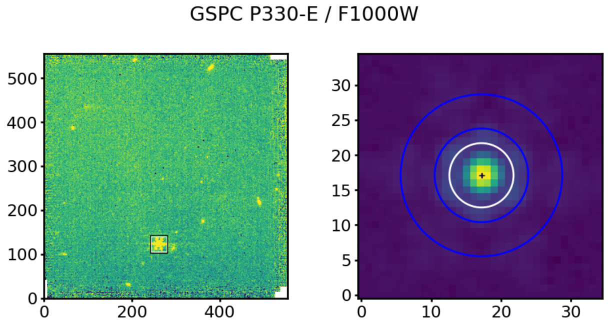

Figure 3. A visualization of the photometric method for GSPC P330E observed with the F1000W imaging band with the BRIGHTSKY subarray. The full mosaic is shown on the left with a white and black box surrounding the target. The right panel zooms in on the target region with the aperture in white, the sky annulus in blue, and the final centroid position marked with a cross. The x and y axis units are pixels, which are $0.11''$ across. The minima and maxima of the color scales differ between the two images.

2.2. *Photometry*

The photometry for each observation was measured using the photutils package (Bradley et al. 2022) from the mosaics using the apertures and aperture corrections from Table 4. The center of the aperture was determined by finding the initial position of the star based on the known coordinates and proper motion, followed by center-of-mass centroiding on the brightest source near this initial position. The photometry accounts for partial pixels in the circular aperture. The uncertainty in the photometry was calculated based on the pipeline propagated uncertainties and includes a second term that gives the uncertainty in the background subtraction based on the measured scatter in the background. A visual example of the photometry is shown in Fig. 3. The photometry in this fixed aperture was then corrected to infinite aperture using the appropriate aperture correction. Table 5 gives the resulting photometry along with additional observational details. This table includes the star name (name), program identification (PID), the source type (srctype), the filter, the subarray, the observation time (time), the central-pixel rate (pixrate), the central-pixel well depth (pixwelldepth), the integration time (inttime), the instrumental flux (iflux), instrumental flux uncertainty (ifluxunc), the instrumental average background per pixel (ibkg), and the equivalent of the last three in physical units (flux, fluxunc, and bkg) using the calibration from section 3.6.

2.3. *Model Predictions*

The predicted flux densities for the hot stars and A dwarfs were determined using CALSPEC[2] models (Bohlin et al. 2014, 2022). For the Solar analogs, models by Rieke et al. (2024) were used. These are the combination of stellar atmosphere models extinguished by dust. See Gordon et al. (2022) for the stellar and dust extinction properties of each star. The band flux densities were calculated using the MIRI band-response functions provided by Pandeia (Pontoppidan et al. 2016). The band flux densities were calculated in $F(\lambda)$ units using Equation 5 from Gordon et al. (2022) and converted to $F(\nu)$ flux densities using the pivot wavelength $\lambda_{\rm ref}$ with the standard conversion (e.g., Equation 11 of Bohlin et al. 2014). This step supports the two common photometric conventions (Gordon et al. 2022).

Table 6. Zero-Magnitude Flux Densities in the Sirius-Vega System

Band	$F(\lambda)$ (ergs Å^{-1} cm^{-2} s^{-1})	$F(\nu)$ (Jy)
F560W	1.090e-12	115.439
F770W	3.340e-13	65.011
F1000W	1.162e-13	38.401
F1065C	8.963e-14	33.562
F1140C	6.929e-14	29.534
F1130W	6.924e-14	29.538
F1280W	4.269e-14	23.368
FND	5.175e-14	28.724
F1500W	2.249e-14	17.020
F1550C	1.976e-14	15.858
F1800W	1.103e-14	11.895
F2100W	6.227e-15	8.981
F2300C	4.383e-15	7.517
F2550W	2.802e-15	6.012

2.4. *Zero-Magnitude Flux Densities in the Sirius-Vega System*

Table 6 provides the flux densities for zero magnitude in the Sirius-Vega system computed in $F(\lambda)$ units as defined for the JWST band fluxes (Gordon et al. 2022) and the $F(\nu)$ values computed as discussed by Bohlin et al. (2014). Magnitudes are not required for the absolute flux calibration, but are used extensively in many studies. They are provided here as a convenience and are based on the known filter bandpasses and the model for Sirius shifted to the brightness of Vega. This approach uses Sirius as the color standard and preserves the historical zero magnitude definition based on Vega (Rieke et al. 2022). The definition of the JWST band fluxes supports both photometric conventions (see Gordon et al. 2022). For the photometric convention that uses color corrections see

---

[2] https://www.stsci.edu/hst/instrumentation/reference-data-for-calibration-and-tools/astronomical-catalogs/calspec

the appropriate JDox page[3] for corrections for a selection of spectral shapes.

3. RESULTS

Following Gordon et al. (2022), the flux calibration factor that converts instrumental DN s^{-1} pixel^{-1} to physical surface brightnesses in MJy sr^{-1} is

$$C = \frac{F}{N_{\rm ap} A_{\rm cor} \Omega_{\rm pix}}. \tag{3}$$

where F is the model flux density in MJy (§2.3), N is the measured flux density in DN s^{-1} pixel^{-1} in a finite aperture (iflux in Table 5), $A_{\rm cor}$ is the aperture correction to an infinite aperture (§2.1), and Ω_{pix} is the average solid angle per pixel (in sr).

Ideally, the flux calibration factor for each band would be a single constant converting instrumental to physical units. As part of this analysis, we have found that the flux calibration depends on both the time of observation and the subarray used. Section 3.1 and 3.3 discuss the dependence on time and subarray, respectively. We did not find that the flux calibration depends significantly on other properties of the detectors or calibration stars. The source parameters investigated include the predicted flux densities, the type of star (hot stars, A dwarfs, and Solar analogs), and measured backgrounds (§3.4). The detector parameters investigated include the central-pixel well depth in DN, the instrumental central-pixel rate in DN s^{-1}, and integration time (§3.5). Section 3.6 quantifies the time- and subarray-dependent flux calibration and accuracy.

3.1. *Temporal Dependence*

The repeatability of a source was monitored through monthly observations of BD+60 1753, an A dwarf that is relatively bright and is known to have very low short-term intrinsic variability (<0.03%, Gordon et al. 2022). The objective is to measure the intrinsic scatter of observations due to variability of the telescope (e.g., PSF) and instrument (e.g., detectors). Focusing on the F770W observations (Fig. 4), the repeatability is measured to be 0.2%, comparable to that measured for the Spitzer/MIPS 24 μm band (Engelbracht et al. 2007) and lower than the 1–2% measured for the IRAC bands (Reach et al. 2005; Bohlin et al. 2011; Krick et al. 2021) .

After the detection of the significant response change at long wavelengths for the MIRI Medium Resolution Spectrometer (MRS) (Law et al. 2024), these observations were expanded to include all imaging filters every month[4]. With this change, the goal of the monitoring of BD+60 1753 expanded to include detecting and measuring any temporal changes in total system response. Combining these expanded observations with observations of the same star taken during JWST Commissioning led to the discovery that the long-wavelength imaging filters also suffer from a temporal degradation in transmission. Fig. 4 shows the relative change in the flux of BD+60 1753 for all 9 imaging bands. In addition, pairs of measurements of δ UMi and HD 37962 are included to add critical measurements in the gap between the end of Commissioning and the start in cycle 2 of the expanded, all-filter observations of BD+60 1753. Both of these additional stars had been observed in multiple long-wavelength filters between days 100 and 200. Repeated observations between days 475 and 500 were taken of both stars to provide a relative measurement. This allowed the earlier measurements to be included in the repeatability measurement by normalizing the latter observations to observations of BD+60 1753 close in time.

The F2550W filter shows a clear degradation in total system responsivity of $\sim$22%. The degradation can be seen in other filters, with the amplitude decreasing monotonically with wavelength to 3% in F1280W. For the shorter-wavelength filters, the degradation is small and generally consistent with very small or no degradation. The imaging response degradation at F2550W of $\sim$22% is significantly smaller than the MRS degradation seen at the equivalent wavelengths (Law et al. 2024). The impact on the S/N of an observation with F2550W is $\sim$11%.

The expanded monitoring of BD+60 1753 measures the repeatability of observations in all imaging filters. As Fig. 4 shows, discrepancies in the repeatability amplitude are lowest for the short-wavelength bands with values of 0.1–0.4% and grow to 1.2% for the F2550W band. These uncertainties set the maximum S/N possible from a single, dithered observation.

3.2. *Anomalous Stars/Observations*

One of the motivations for observing a sample of stars is to identify stars that are not suitable for absolute flux calibration. We found one star that fell into this category. In addition, a few observations in specific filters were found to be significantly deviant from the average.

The A dwarf HD 180609 shows a clear signature of a debris disk, with an observed excess above the model prediction for long-wavelength bands that increases with wavelength. The signature of such an excess is a decreasing calibration factor as a function of wavelength, and this is clearly seen for this star. This makes this star unsuitable for flux calibration measurements and it was removed from all analyses except for the subarray dependence as it is the only star observed in all filters with SUB128 (see below). Debris disks have appeared in samples of presumably well-vetted standard stars before. In the Spitzer (Werner et al. 2004) Infrared Spectrometer (Houck et al. 2004) absolute flux program, four of the 20 A dwarf standards had a clear debris disk, plus three suspects, along with one of the 30 K giant standards (Sloan et al. 2004, 2015). In the Spitzer Mid-Infrared Instrument (Rieke et al. 2004) absolute flux program, one A dwarf and one K giant were found to have the signature of a debris disk (Gordon et al. 2007). The difficulty of avoiding these occa-

---

[3] To be added to JDox very soon

[4] https://www.stsci.edu/contents/news/jwst/2023/temporal-behavior-of-the-miri-reduced-count-rate

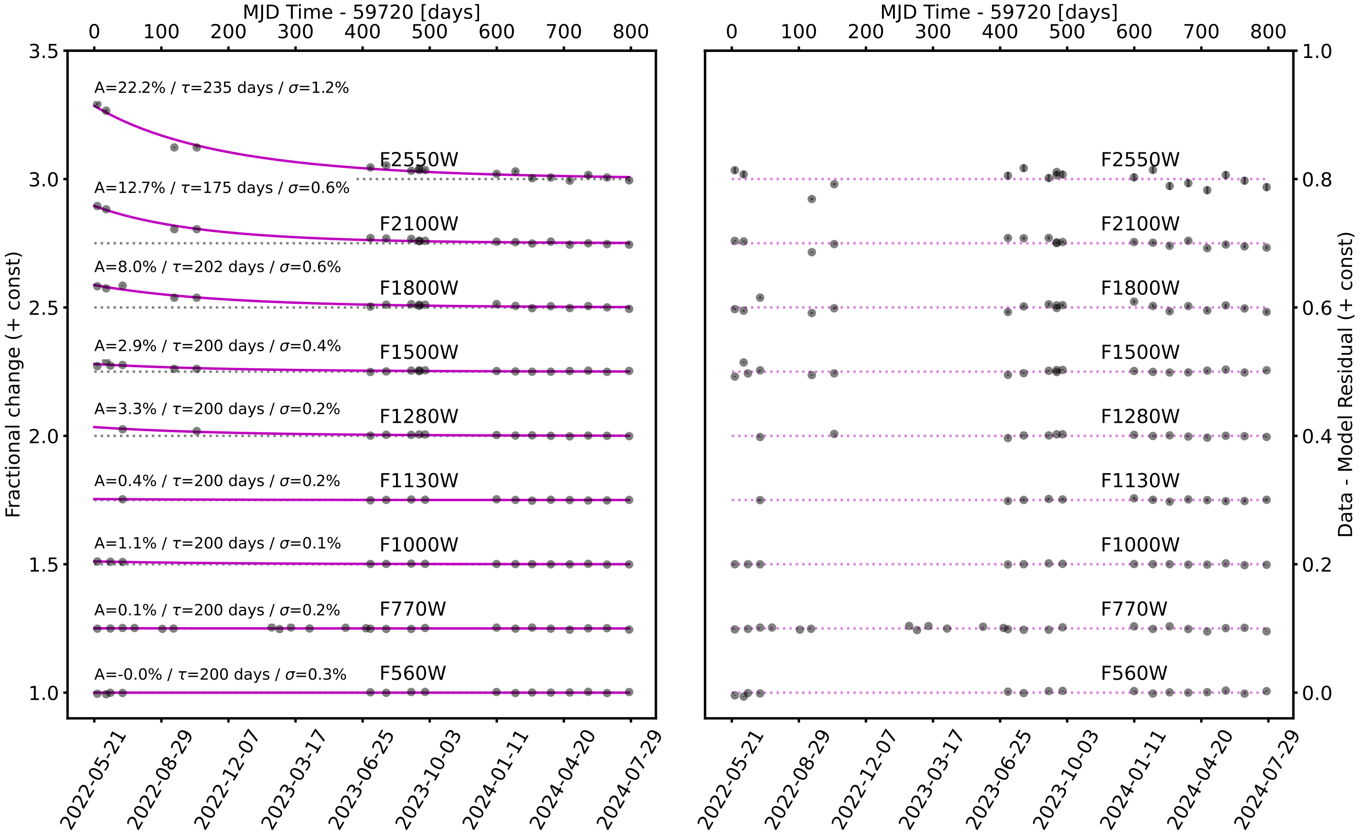

Figure 4. Left: The time-dependent behavior of the repeated observations of BD+60 1753 plus two other stars for all the imaging filters. An exponential model fit to the observations in each band is plotted in this panel as the solid purple line. The dotted line gives the value after the modeled exponential has fully decayed. The amplitude A, the time constant τ, and standard deviation σ around the exponential fit are given on the left. Right: The residuals after subtraction of the exponential model.

sional anomalies drives the need for observing a sample of stars of each stellar type.

As part of computing the calibration factors, some observations were found to be significantly different than average. Often these deviant observations were seen for a single observation for a star, with all the other observations for the same star being consistent with the average. The deviant observations are indicated in the calibration factor plots in the rest of this paper. There was one star where all its observations were flagged as deviant. This was C26202 that was observed in F560W, F770W, and F1000W and the deviations seen were both above and below the average. The reason for all the observations being deviant is under investigation.

Table 7. Subarray Dependence

Subarray	$D_{\rm SA}$
FULL	1.000
BRIGHTSKY	1.005
SUB256	0.980
SUB128	1.000
SUB64	0.966

3.3. *Subarray Dependence*

Observations for absolute flux calibration are taken with different subarrays so that both faint and bright targets can be observed. The MIRI Imager has five subarrays including FULL using all the detector pixels and four smaller subarrays (BRIGHTSKY, SUB256, SUB128, SUB64) with each successively reducing the area read by a factor of four (Ressler et al. 2015). Measuring potential differences in the observed flux densities in different subarrays is important to ensuring a consistent calibration. Possible causes of variations between subarrays include different readout patterns, transients associated with switching subarrays, and flatfield spatial errors as the subarrays are in different detector locations (Wright et al. 2023; Dicken et al. 2024).

Dedicated observations to measure variations in the flux calibration with subarray were taken in two filters with two different stars. 2MASS J17571324+6703409 was ob-

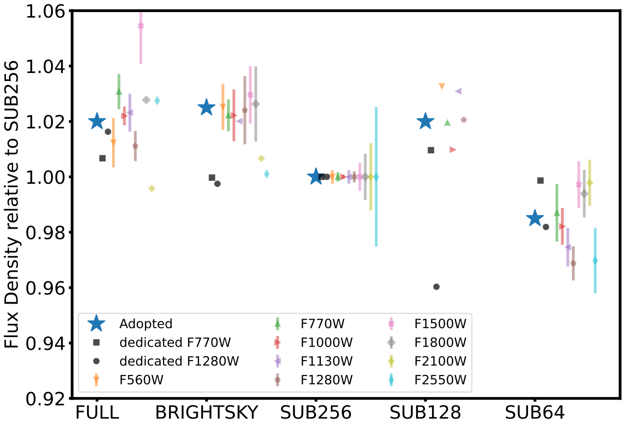

Figure 5. The fractional change in flux density relative to SUB256 for each subarray using a variety of observations. The dedicated subarray transfer observations taken in F770W and F1280W are simple ratios of the measured flux densities where multiple measurements in the same subarray were averaged if available. All of the flux-calibration observations were used to measure equivalent ratios using the weighted average calibration factors for each subarray and band. The uncertainties for these ratios are the weighted standard deviation of the mean. No error bars are shown for three or fewer observations. The blue stars are the adopted relative subarray throughputs.

served back-to-back in the F770W band for all five subarrays. 2MASS J18022716+6043356 was observed back-to-back in the F1280W band for all five subarrays, with the FULL and SUB64 subarrays observed multiple times. For the F1280W measurements, the FULL frame observations were taken at the beginning and end of the observation sequence to check that any changes seen did not depend on the order of the observations. Fig. 5 shows the flux density in each subarray relative to that observed in the SUB256 subarray. For all but the SUB128 subarray, these two sets of measurements agree well. For the SUB128 subarray, they differ by ∼4%, but the cause is not yet known, and additional dedicated observations will be needed to determine it.

The rest of the observations can be used to probe the subarray dependence as well. First, the weighted average calibration factor and uncertainty for each subarray in each band is calculated after correcting for the known temporal dependence. The weighting was such that each star had equal weight in the average (e.g., a star with n observations has its observations each given a weight of n^{-1}). The equivalent measurement can then be computed by taking the ratio of the SUB256 subarray calibration factor to that measured in the other subarrays. This ratio has the SUB256 calibration factor in the numerator as the measured flux densities are in the denominator of the calibration factor calculation. The SUB256 subarray was used as the reference as it was the subarray with the most observations with flux calibration data in all bands.

Fig. 5 shows the resulting ratios. For FULL and SUB64, these ratios agree well with those measured from the dedicated observations. For BRIGHTSKY, the ratios disagree for both the F770W and F1280W dedicated measurements when considering the averages based on >3 observations. For SUB128, the ratios agree well with the dedicated F770W observations, but not those taken with F1280W. The SUB128 ratio values are dominated by HD 180609, a star with a clear signature of a debris disk in F1500W and longer bands (see Section 3.2). We have included the F1280W and shorter bands for this star in the analysis only for the subarray dependence because it is the only star observed in SUB128 for all bands. In the end, the SUB128 dependence is the same as the FULL subarray, resulting in no SUB128 correction compared to FULL.

In summary, the dedicated subarray observations for the SUB128 subarray do not agree and these dedicated observations do not agree with the ratios based on calibration factors for the BRIGHTSKY subarray. The two sets of observations are consistent enough that we can conclude that the subarrays differ significantly. Visually examining Fig. 5, we have adopted subarray dependencies mainly influenced by the calibration factor ratios, but also taking into account the dedicated observations. The calibration factor ratios are preferred because (1) they are based on many more observations than the dedicated subarray observations, and (2) the dedicated subarray observations could be impacted by subarray switching transients. The subarray was measured relative to SUB256, because SUB256 was well measured in all bands. It is preferable to have the subarray dependence relative to the FULL subarray that is used for most MIRI imaging observations. Hence, the $D_{\rm SA}$ dependence as given in Table 7 is given relative to FULL frame by dividing the adopted values shown in Fig. 5 by the adopted FULL value. Thus, $D_{\rm SA}$ gives the throughput for each subarray relative to the FULL frame.

3.4. *Source Dependencies*

Fig. 6 shows how the F1280W calibration factors for each observation depend on multiple source parameters. Investigating if the calibration factor depends on properties of the source is important to test that the calibration factor is applicable to as wide a range of observations as can be tested. The weighted averages and uncertainties were computed as described in §3.3.

The plot versus model flux density shows that the calibration is constant for sources from 0.2 to 200 mJy. The lack of a dependence on flux density in all but one of the bands (see appendix Fig. 10) leads to two conclusions. First, the MIRI detectors do not suffer from significant non-linearities due to a dependence on flux density (Bohlin et al. 2006; de Jong et al. 2006). Second, the known brighter-fatter effect (Argyriou et al. 2023) is not affecting the photometry in the aperture used. The one possible exception to this result is the FND band, which shows a small trend with predicted flux density (as discussed further in the next subsection).

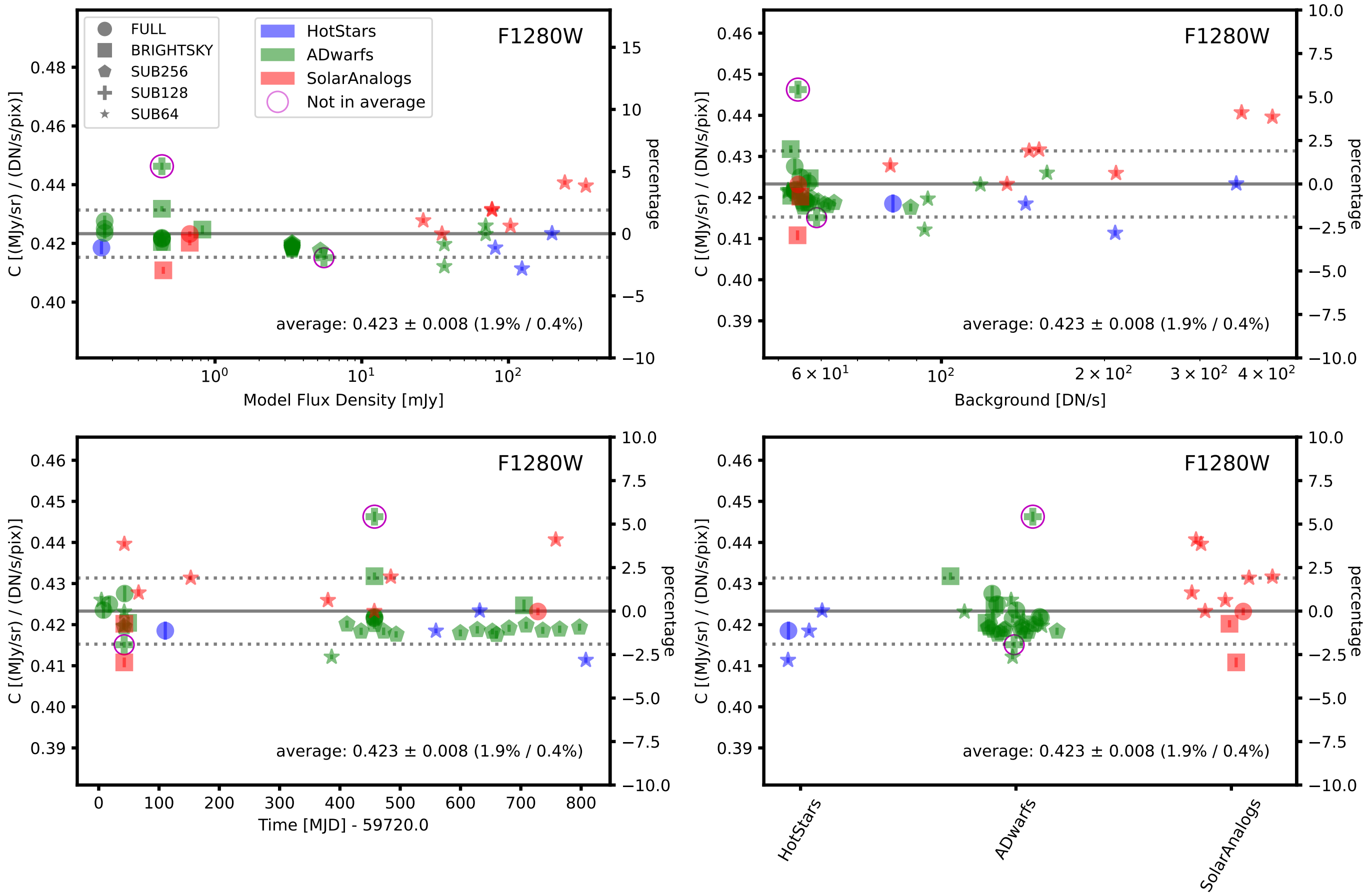

Figure 6. The F1280W calibration factors plotted as a function of the source predicted flux density, measured background, observation time, and source type. The calibration factors are corrected for the time and subarray dependencies. Each point represents one observation for one star. The colors and symbols to distinguish different types of stars and subarrays are the same in all panels. While the observation of HD 180609 is within the scatter for this band, it is flagged and not used (§3.2). In addition, one observation is flagged as $> 3.5\sigma$ from the weighted average and not used (§3.2). The solid horizontal gray line gives the weighted average in each panel, with the $\pm 1\sigma$ standard deviations as dotted gray lines. The average calibration factors and uncertainties are given in the lower right of each plot. The percentage standard deviation and standard deviation of the mean are given in parentheses as well.

Another possible dependence could be on the measured background. The background affects all pixels similarly unlike a point source with its strong gradients in the illumination between pixels. The plot versus background for F1280W and for all the bands (see appendix Fig. 11) shows no dependence on such uniform illumination.

The temporal dependence determined from repeated observations of mainly one star discussed in §3.1 is tested using all the observations in the lower left plot of this figure. The plot shows that the temporal correction is working well for all observations for F1280W and, in fact, all bands (see appendix Fig. 12).

The lower right panel in Fig. 6 probes the dependence on the type of calibration star. No obvious dependence on type of star is found for F1280W or for the other bands (see appendix Fig. 13). To quantify the difference between source types, the average calibration factors for each band were computed by source type. Fig. 7 plots the ratios between these values and the average calibration factors per band for all source types (in colors), along with the weighted averages of all bands per source type (in black) and error bars that represent the 5σ standard deviation. The averages for all the types of stars are within 5σ of unity, indicating no significant difference in the calibration factors between types. These results indicate that the calibration does not depend systematically on source type.

3.5. *Detector Dependencies*

The calibration factor can depend on detector parameters as has already been shown for subarrays. Fig. 8 plots the F1280W calibration factors after correction for the time and subarray dependence as a function of the detector parameters central-pixel rate, central-pixel well depth, integration time, and subarray. The weighted averages and uncertainties were computed as described in §3.3.

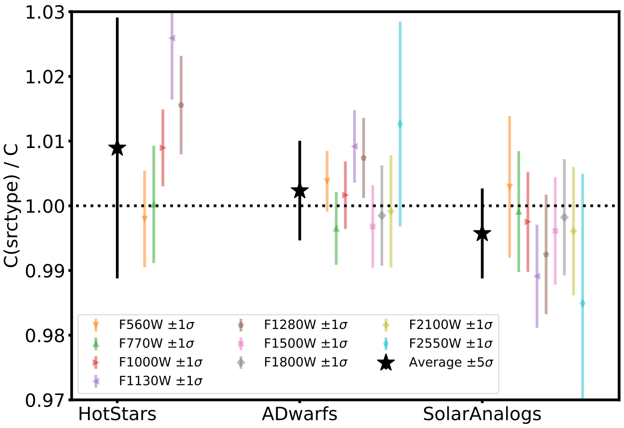

Figure 7. The ratio of the average calibration factor for each band for each source type versus the average calibration factor per band for all source types. Only bands with > 3 individual measurements are shown as this is required to measure an uncertainty. The error bars for the individual bands are one σ standard deviations. Black stars and vertical lines depict the weighted average of all bands and five times the standard deviation of the mean (5σ).

The dependence on the rate of arriving photons is investigated in the upper left of Fig. 8. This panel closely resembles the plot in the previous section versus model flux, except that the central-pixel rate is used given in instrumental DN s^{-1}. As in Fig. 6, no clear dependence is seen for F1280W or any of the other filters except for the FND filter (see appendix Fig. 14).

The central-pixel well depth probes the accuracy of the applied non-linearity correction. The lower left panel in Fig. 8 shows no clear dependence on central-pixel well depth, indicating that the non-linearity correction is quite accurate for F1280W and all bands except the FND (see appendix Fig. 15).

The FND band shows a trend with predicted flux density, central-pixel rate, and central-pixel well depth. This result is surprising, because all of the wavelengths covered by the FND band are covered with other filters that do not show such trends. A possible origin of the FND behavior may be the result of its very wide bandpass, with a width of 6.7 μm centered on 12.9 μm. The MIRI non-linearity correction is known to depend on wavelength (Morrison et al. 2023), with longer-wavelength bands having a different non-linearity that shorter-wavelength bands. The FND observations were processed using the non-linearity correction for bands F1280W and shorter, but they may possibly have a different non-linearity as the red end of the band extends well beyond the F1280W band. Future non-linearity work will investigate this possible explanation.

The upper right panel in Fig. 8 probes the dependence of calibration factor on the integration time, which could be caused by reset-induced transients that occur near the beginning of a ramp and could impact shorter ramps more than longer ramps. No clear dependence on integration times from 0.5 to 40 s for F1280W is found. When including all the bands (see appendix Fig. 16), no significant dependence is seen for integrations times from 0.5 to near 300 s. This lack of dependencies indicates that the reset transients are not significantly affecting the calibration factors.

Finally, the accuracy of the subarray dependence derived in §3.3 is tested for F1280W in the lower right panel of Fig. 8. This plot clearly shows that the subarray correction is accurate, which is not surprising as it was derived partially with these observations. This result is also true for all of the other bands, as can be seen in the appendix Fig. 17. The lack of a sufficient number of observations prevented a similar check for the SUB128 subarray. The only star observed in all bands with SUB128 has a debris disk (§3.2).

3.6. *Calibration Factors*

The average calibration factors are computed after correcting for the dependencies on time and subarray so that all measurements could be used. Averaging measurements of calibration factors made for different stars results in a more accurate flux calibration. A single star has been found empirically to be modeled to an accuracy of ∼2% (Bohlin et al. 2014) and, hence, to improve on this accuracy, multiple stars need to be averaged. In addition, any single star can have properties that make it systematically challenging to model. The debris disk found as part of this work is one example. The most famous case of such confounding issues is for Vega that is so rapidly rotating that it has a large gradient in its stellar temperature from pole to equator *and* it has a debris disk clearly seen in the near- and mid-IR (Aumann et al. 1984; Su et al. 2005; Aufdenberg et al. 2006). Hence, observing multiple stars allows for (1) the removal of such confounding sources and (2) averaging the remainder to improve the flux-calibration accuracy.

Combining the time and subarray dependencies with the average factors, the calibration factor as a function of time and subarray is then

$$C(t) = \frac{A + B \exp\left[-(t - t_o)/\tau\right]}{D_{\mathrm{SA}}} \tag{4}$$

where t is the time in MJD, A gives the calibration factor at infinite time after the exponential has fully decayed, B is the amplitude of the time dependent term, $t_o = 59720\ d$, τ is the time constant in days, and D_{SA} is the relative change with subarray. Tables 8 and 7 give the coefficients for each band and subarray, respectively. For the coronagraphic and FND filters, the temporal dependence was calculated by interpolating between the two imaging filters to either side in wavelength and weighting by the distance in wavelength. The number of stars contributing to the calibration factors n_{stars} can be non-integral if some of the observations for a star are not used in the average. The final column gives the percentage repeatability $\sigma(\mathrm{repeat})$ as measured in §3.1.

Fig. 9 shows the refinement of the calibration factor measurements over time. The first delivery in 2022 was based

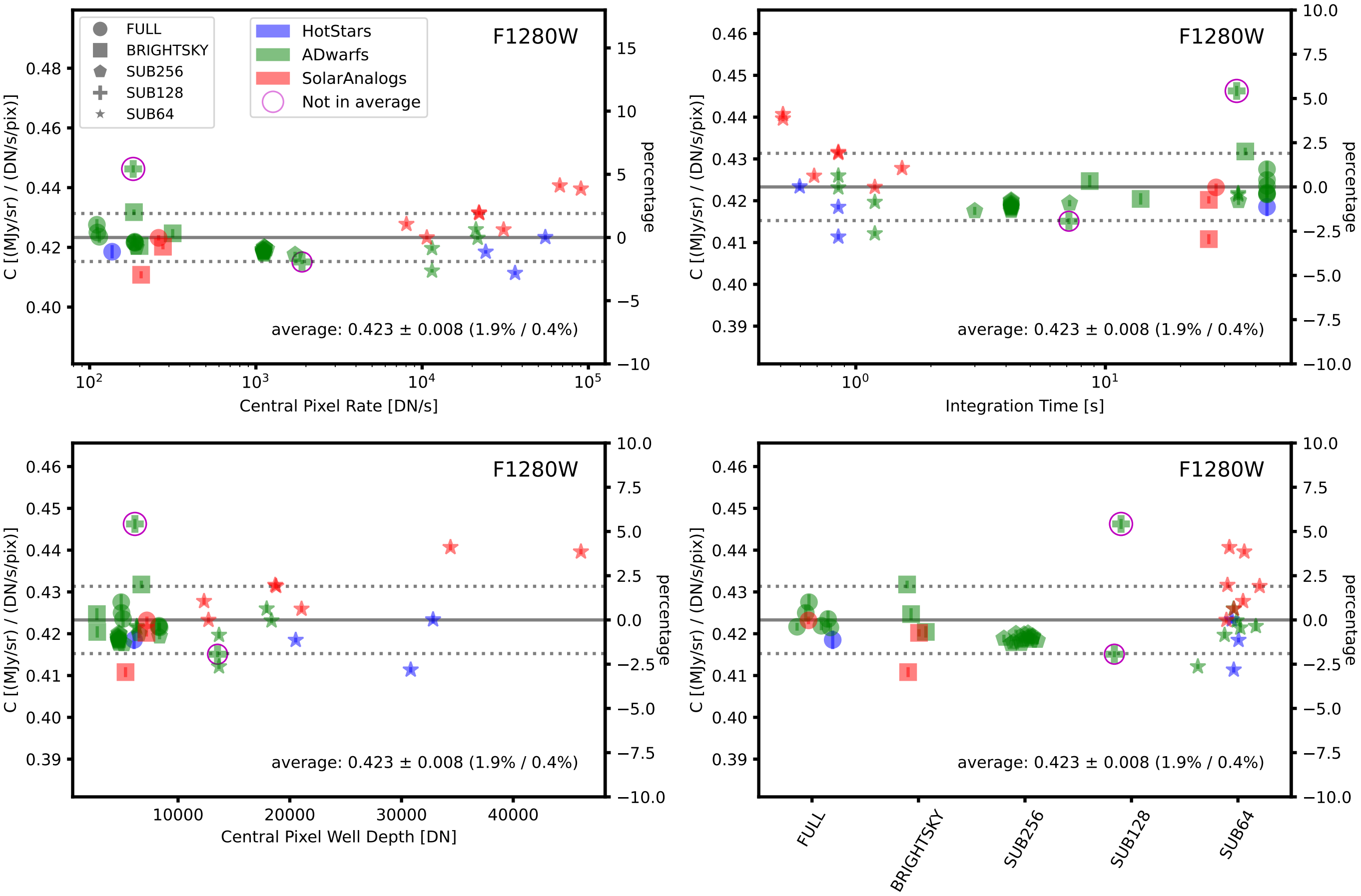

Figure 8. The calibration factor versus the detector parameters central-pixel rate, integration time, central-pixel well depth, and subarray. The calibration factors plotted have been corrected for the temporal and subarray dependencies. Different colors and symbols indicate different types of stars and subarrays. While the observation of HD 180609 is within the scatter for this band, it is flagged and not used (§3.2). In addition, one observation is flagged as $> 3.5\sigma$ from the weighted average and not used (§3.2). The horizontal gray solid line shows weighted average, with dotted lines for the $\pm 1\sigma$ standard deviation. The calibration factors and uncertainties are given in the lower right of each plot. The percentage standard deviation and standard deviation of the mean are in parentheses as well.

on Commissioning observations of 1–2 stars and the instrument knowledge at that time. The second delivery in 2023 reflected observations of a significantly larger sample of stars and, critically, a better understanding of the instrument, especially how to model the PSF. For this second delivery, the PSFs were modeled with a combination of observed PSFs for the cores and model PSFs for the wings (like §2.1). In particular, the changes seen in the F560W and F770W bands were due to the inclusion of a model for the cruciform artifact that significantly affects these two bands. In addition, the large change for all the coronagraphic bands resulted from correcting an error in the normalization of the model PSFs. The third delivery is based on the results reported in this work and includes more observations and the addition of the subarray correction.

The standard deviation of the calibration factor $\sigma(CF)$ ranges from 0.32 to 0.98% for the imaging bands and 0.42 to 0.90% for the coronagraphic bands. The $\sigma(CF)$ expressed as a percentage gives the contribution that the absolute flux calibration makes to the uncertainty on any measurement expressed in physical units. The repeatability uncertainty, $\sigma(\text{repeat})$, gives the uncertainty for any single measurement taken with a similar four-point dither measurement of a point source. In other words, these two uncertainties should be combined in quadrature with the uncertainties based on read, photon, and flatfield uncertainties reported by the JWST pipeline.

The uncertainties quoted are correct for measurements of a well-exposed point source, in other words observations like those taken for the flux-calibration stars. In particular, the uncertainties for resolved sources that focus on surface brightnesses are larger, because the surface brightness uncertainties include the uncertainties in the aperture corrections to infinite aperture. The uncertainties quoted in §2.1 for the aperture corrections are small and are based mainly on scatter between similar measurements. These uncertainties do not probe the systematic uncertainties related to effects not present in the PSF models. In particular, the modeling of the cruciform for

Table 8. Calibration Factor Info

Band	$A^\star$	$B^\star$	B (%)	τ (days)	$\sigma(CF)^\star$	$\sigma(CF)$ (%)	n_{stars}	σ(repeat) (%)
Imaging								
F560W	0.4496	0.0000	0.0	200.0	0.00166	0.37	11.75	0.27
F770W	0.2579	-0.0001	0.1	200.0	0.00096	0.37	15.00	0.25
F1000W	0.3488	-0.0038	1.1	200.0	0.00111	0.32	20.00	0.08
F1130W	1.0898	-0.0042	0.4	200.0	0.00520	0.48	19.00	0.16
F1280W	0.4233	-0.0140	3.3	200.0	0.00185	0.44	18.89	0.20
FND	41.5591	-1.3650	3.3	200.0	0.39411	0.95	10.00	···
F1500W	0.3703	-0.0107	2.9	200.0	0.00176	0.48	21.00	0.45
F1800W	0.5067	-0.0407	8.0	201.7	0.00300	0.59	20.00	0.60
F2100W	0.4389	-0.0557	12.7	175.0	0.00290	0.66	17.00	0.59
F2550W	0.9064	-0.2011	22.2	235.4	0.00888	0.98	16.00	1.20
Corongraphy								
F1065C	3.1125	-0.0234	0.8	200.0	0.01313	0.42	5.00	···
F1140C	2.8703	-0.0112	0.4	200.0	0.02100	0.73	5.00	···
F1550C	3.8974	-0.1441	3.7	200.3	0.02841	0.73	4.00	···
F2300C	1.1106	-0.1852	16.7	200.4	0.00996	0.90	4.00	···

*Units of (MJy sr^{-1}) / (DN s^{-1} pixel^{-1}).

the F560W and F770W bands is known to be incomplete, which contributes an additional uncertainty estimated to be on the order of 3% based on an independent analysis using highly saturated PSFs.

4. SUMMARY

The absolute flux calibration for MIRI Imaging and Coronagraphy is based on over two years of dedicated observations. These observations include stars of three different types: eight hot stars, eleven A dwarfs, and nine Solar analogs.

The main components of the calculated calibration factors are the predicted fluxes for each star, aperture photometry for each observation in instrumental units, and aperture corrections to provide the correction to infinite aperture. Well-exposed, isolated stars observed as part of the absolute flux calibration were combined with model PSFs and used to measure the enclosed energy curves, determine the radii, sky annuli, and aperture corrections for aperture photometry. Automated routines[5] produced all of the aperture photometry, allowing for straightforward updating of the photometry with new JWST pipeline versions and calibration reference files. The predicted fluxes for each star were determined by integrating the predicted fluxes from models with the appropriate band response functions.

Calibration factors for each observation were computed and examined for any dependencies. Dedicated repeat measurements of one star supplemented by observations of two other stars revealed that the longer-wavelength imaging filters suffer from a time-dependent loss in total system response. This loss is fit well with an exponential model with a time constant around 200 days with scatter less than 1% for all but the F2550W band. F1280W and longer-wavelength bands were seen to have a significant loss, starting at 3% and rising to 22% at F2550W. After correcting for the temporal response loss, a subarray dependence was found by combining dedicated observations of two stars observed in all of the subarrays with all the average calibration factor measurements for each subarray. The dependence relative to FULL frame ranges from no change to 3.4% for the SUB64 subarray.

A search for dependencies with other source and detector parameters reveals no significant dependencies after correction for the known temporal and subarray dependencies. Source dependencies checked were versus predicted model flux, measured background, and type of star. In addition, the accuracy of the time-dependent correction was confirmed to work well for all the observations. The detector dependencies were checked versus the central-pixel rate, central-pixel well depth, and the integration time. In addition, the accuracy of the subarray correction was tested and found to work well.

---

[5] https://github.com/STScI-MIRI/ImagingFluxCal

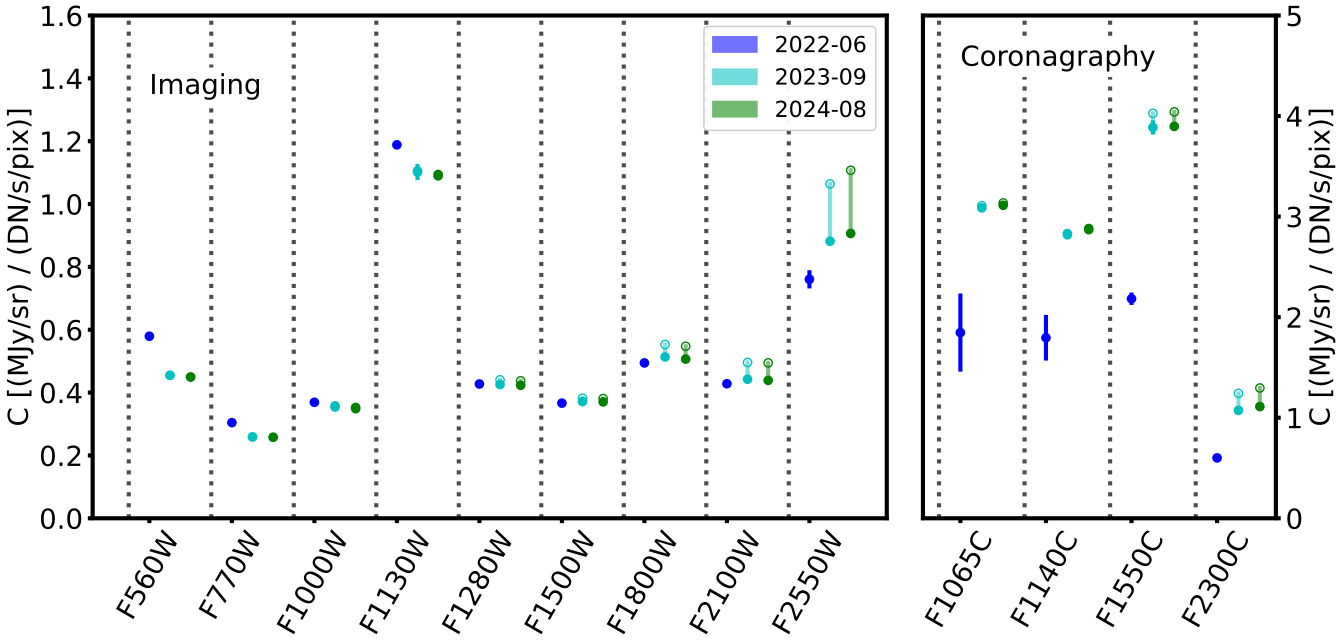

Figure 9. The delivered calibration factors used by the pipeline are plotted versus time for all bands except FND. The FND calibration has been determined for the first time with this work and so is not plotted. For the two most recent deliveries, the time-dependent variation is shown as a solid symbol (start of observations) connected to an open symbol (asymptotic value after all expected change). The changes reflect the improved calibration factor measurements with more observations and a better understanding of the telescope and instrument.

The time- and subarray-dependent calibration factors for each imaging and coronagraphic band are reported and have been delivered for use in the JWST pipeline. For the first time, this work provides the calibration factor for the wide neutral-density FND band that is used for target acquisition. The scatter in the calibration factors from individual stars ranges from 1 to 4% depending on the band. The uncertainty in the average calibration factors ranges from 0.3 to 1.0% depending on the band. The uncertainties on the calibration factors are lower than pre-launch expectations (e.g., “requirements”) and support a wide range of astrophysical investigations including those needing percent-level or better absolute-flux calibration.

The imaging and coronagraphic flux calibration will continue to improve as additional observations of absolute flux calibration targets are taken and the knowledge of the MIRI instrument improves.

This work is based [in part] on observations made with the NASA/ESA/CSA James Webb Space Telescope. The data were obtained from the Mikulski Archive for Space Telescopes at the Space Telescope Science Institute, which is operated by the Association of Universities for Research in Astronomy, Inc., under NASA contract NAS 5-03127 for JWST. These observations are associated with programs #1027, 1045, 1523, 1524, 1536, 1537, 1538, 1539, 4488, 4496, 4497, 96 4498, 4499, 4578, and 6607. The following National and International Funding Agencies funded and supported the MIRI development: NASA; ESA; Belgian Science Policy Office (BELSPO); Centre Nationale d’Etudes Spatiales (CNES); Danish National Space Centre; Deutsches Zentrum fur Luftund Raumfahrt (DLR); Enterprise Ireland; Ministerio De Economi´a y Competividad; Netherlands Research School for Astronomy (NOVA); Netherlands Organisation for Scientific Research (NWO); Science and Technology Facilities Council; Swiss Space Office; Swedish National Space Agency; and UK Space Agency. MD acknowledges support from the Research Fellowship Program of the European Space Agency (ESA).

Software: Astropy (Astropy Collaboration et al. 2013, 2018, 2022), Photutils (Bradley et al. 2022)

REFERENCES

Argyriou, I., Lage, C., Rieke, G. H., et al. 2023, A&A, 680, A96, doi: 10.1051/0004-6361/202346490

Astropy Collaboration, Robitaille, T. P., Tollerud, E. J., et al. 2013, A&A, 558, A33, doi: 10.1051/0004-6361/201322068

Astropy Collaboration, Price-Whelan, A. M., Sipőcz, B. M., et al. 2018, AJ, 156, 123, doi: 10.3847/1538-3881/aabc4f

Astropy Collaboration, Price-Whelan, A. M., Lim, P. L., et al. 2022, apj, 935, 167, doi: 10.3847/1538-4357/ac7c74

Aufdenberg, J. P., Mérand, A., Coudé du Foresto, V., et al. 2006, ApJ, 645, 664, doi: 10.1086/504149

Aumann, H. H., Gillett, F. C., Beichman, C. A., et al. 1984, ApJL, 278, L23, doi: 10.1086/184214

Boccaletti, A., Lagage, P. O., Baudoz, P., et al. 2015, PASP, 127, 633, doi: 10.1086/682256

Boccaletti, A., Cossou, C., Baudoz, P., et al. 2022, A&A, 667, A165, doi: 10.1051/0004-6361/202244578

Bohlin, R. C., Gordon, K. D., & Tremblay, P. E. 2014, PASP, 126, 711, doi: 10.1086/677655

Bohlin, R. C., Krick, J. E., Gordon, K. D., & Hubeny, I. 2022, AJ, 164, 10, doi: 10.3847/1538-3881/ac6fe1

Bohlin, R. C., Riess, A., & de Jong, R. 2006, NICMOS Count Rate Dependent Non-Linearity in G096 and G141, Instrument Science Report NICMOS 2006-002, 21 pages

Bohlin, R. C., Gordon, K. D., Rieke, G. H., et al. 2011, AJ, 141, 173, doi: 10.1088/0004-6256/141/5/173

Bradley, L., Sipőcz, B., Robitaille, T., et al. 2022, astropy/photutils: 1.5.0, 1.5.0, Zenodo, doi: 10.5281/zenodo.6825092

de Jong, R. S., Bergeron, E., Riess, A., & Bohlin, R. 2006, NICMOS count-rate dependent nonlinearity tests using flatfield lamps, Instrument Science Report NICMOS 2006-001, 14 pages

Dicken, D., Marín, M. G., Shivaei, I., et al. 2024, A&A, 689, A5, doi: 10.1051/0004-6361/202449451

Engelbracht, C. W., Blaylock, M., Su, K. Y. L., et al. 2007, PASP, 119, 994, doi: 10.1086/521881

Gardner, J. P., Mather, J. C., Abbott, R., et al. 2023, PASP, 135, 068001, doi: 10.1088/1538-3873/acd1b5

Gáspár, A., Rieke, G. H., Guillard, P., et al. 2021, PASP, 133, 014504, doi: 10.1088/1538-3873/abcd04

Gordon, K. D., Engelbracht, C. W., Fadda, D., et al. 2007, PASP, 119, 1019, doi: 10.1086/522675

Gordon, K. D., Bohlin, R., Sloan, G. C., et al. 2022, AJ, 163, 267, doi: 10.3847/1538-3881/ac66dc

Houck, J. R., Roellig, T. L., van Cleve, J., et al. 2004, ApJS, 154, 18, doi: 10.1086/423134

Krick, J. E., Lowrance, P., Carey, S., et al. 2021, AJ, 161, 177, doi: 10.3847/1538-3881/abe390

Law, D. R., Argyriou, I., Gordon, K. D., et al. 2024, AJ, in prep

Libralato, M., Argyriou, I., Dicken, D., et al. 2024, PASP, 136, 034502, doi: 10.1088/1538-3873/ad2551

Morrison, J. E., Dicken, D., Argyriou, I., et al. 2023, PASP, 135, 075004, doi: 10.1088/1538-3873/acdea6

Perrin, M. D., Pueyo, L., Gorkom, K. V., et al. 2018, in Space Telescopes and Instrumentation 2018: Optical, Infrared, and Millimeter Wave, ed. M. Lystrup, H. A. MacEwen, G. G. Fazio, N. Batalha, N. Siegler, & E. C. Tong, Vol. 10698, International Society for Optics and Photonics (SPIE), 1069809, doi: 10.1117/12.2313552

Perrin, M. D., Sivaramakrishnan, A., Lajoie, C.-P., et al. 2014, in Society of Photo-Optical Instrumentation Engineers (SPIE) Conference Series, Vol. 9143, Space Telescopes and Instrumentation 2014: Optical, Infrared, and Millimeter Wave, ed. J. Oschmann, Jacobus M., M. Clampin, G. G. Fazio, & H. A. MacEwen, 91433X, doi: 10.1117/12.2056689

Perrin, M. D., Soummer, R., Elliott, E. M., Lallo, M. D., & Sivaramakrishnan, A. 2012, in Society of Photo-Optical Instrumentation Engineers (SPIE) Conference Series, Vol. 8442, Space Telescopes and Instrumentation 2012: Optical, Infrared, and Millimeter Wave, ed. M. C. Clampin, G. G. Fazio, H. A. MacEwen, & J. Oschmann, Jacobus M., 84423D, doi: 10.1117/12.925230

Pontoppidan, K. M., Pickering, T. E., Laidler, V. G., et al. 2016, in Society of Photo-Optical Instrumentation Engineers (SPIE) Conference Series, Vol. 9910, Observatory Operations: Strategies, Processes, and Systems VI, ed. A. B. Peck, R. L. Seaman, & C. R. Benn, 991016, doi: 10.1117/12.2231768

Reach, W. T., Megeath, S. T., Cohen, M., et al. 2005, PASP, 117, 978, doi: 10.1086/432670

Ressler, M. E., Sukhatme, K. G., Franklin, B. R., et al. 2015, PASP, 127, 675, doi: 10.1086/682258

Rieke, G. H., Schlawin, E., Proffitt, C. R., & Willmer, C. 2024, AJ, 167, 213, doi: 10.3847/1538-3881/ad24f7

Rieke, G. H., Su, K., Sloan, G. C., & Schlawin, E. 2022, AJ, 163, 45, doi: 10.3847/1538-3881/ac3b5d

Rieke, G. H., Young, E. T., Engelbracht, C. W., et al. 2004, ApJS, 154, 25, doi: 10.1086/422717

Rieke, G. H., Wright, G. S., Böker, T., et al. 2015, PASP, 127, 584, doi: 10.1086/682252

Sloan, G. C., Herter, T. L., Charmandaris, V., et al. 2015, AJ, 149, 11, doi: 10.1088/0004-6256/149/1/11

Sloan, G. C., Charmandaris, V., Fajardo-Acosta, S. B., et al. 2004, ApJL, 614, L77, doi: 10.1086/425324

Su, K. Y. L., Rieke, G. H., Misselt, K. A., et al. 2005, ApJ, 628, 487, doi: 10.1086/430819

Werner, M. W., Roellig, T. L., Low, F. J., et al. 2004, ApJS, 154, 1, doi: 10.1086/422992

Wright, G. S., Rieke, G. H., Glasse, A., et al. 2023, PASP, 135, 048003, doi: 10.1088/1538-3873/acbe66

APPENDIX

A. ALL CALIBRATION FACTOR PLOTS

Figs. 10–17 show the calibration factor plots for all the imaging and coronagraphic bands for all the source and detector parameters discussed in Sections 3.4 and 3.5. These allow the behaviors discussed in the above referenced sections to be investigated for all bands as well as a straightforward comparison of behaviors between bands.

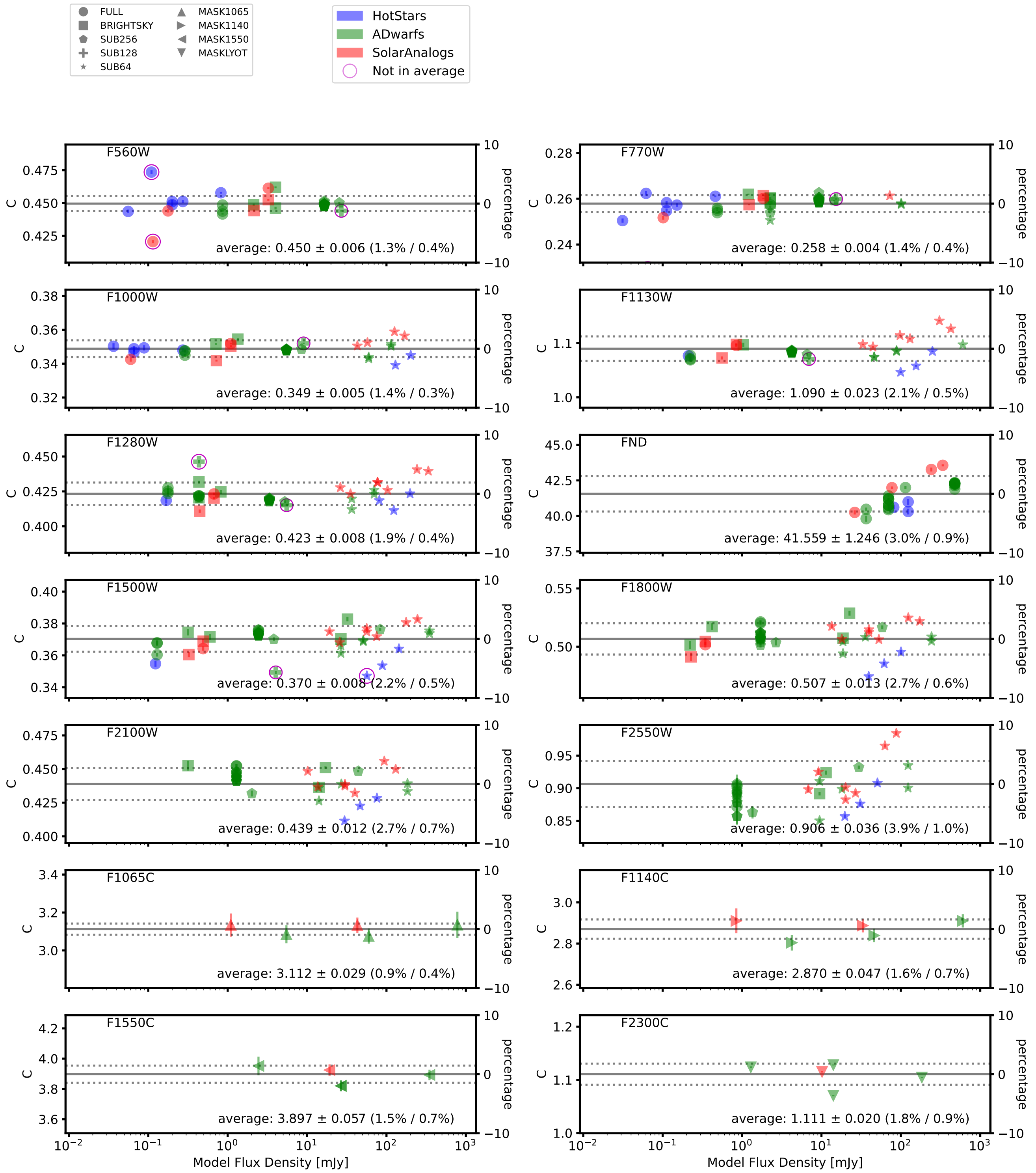

Figure 10. The calibration factors as a function of model flux densities for every observation for the imaging and coronagraphic filters. The temporal response loss and subarray variations have been corrected. While the observations of HD 180609 are within the scatter for some bands, it is flagged in all bands and not used (§3.2). In addition, some observations are flagged as $> 3.5\sigma$ from the weighted average and not used (§3.2). A horizontal solid gray line and the parallel dotted lines give the weighted average $\pm 1\sigma$ standard deviation. The calibration factors and uncertainties are given in the lower right of each plot, and the percentage standard deviation and standard deviation of the mean are given in parentheses as well.

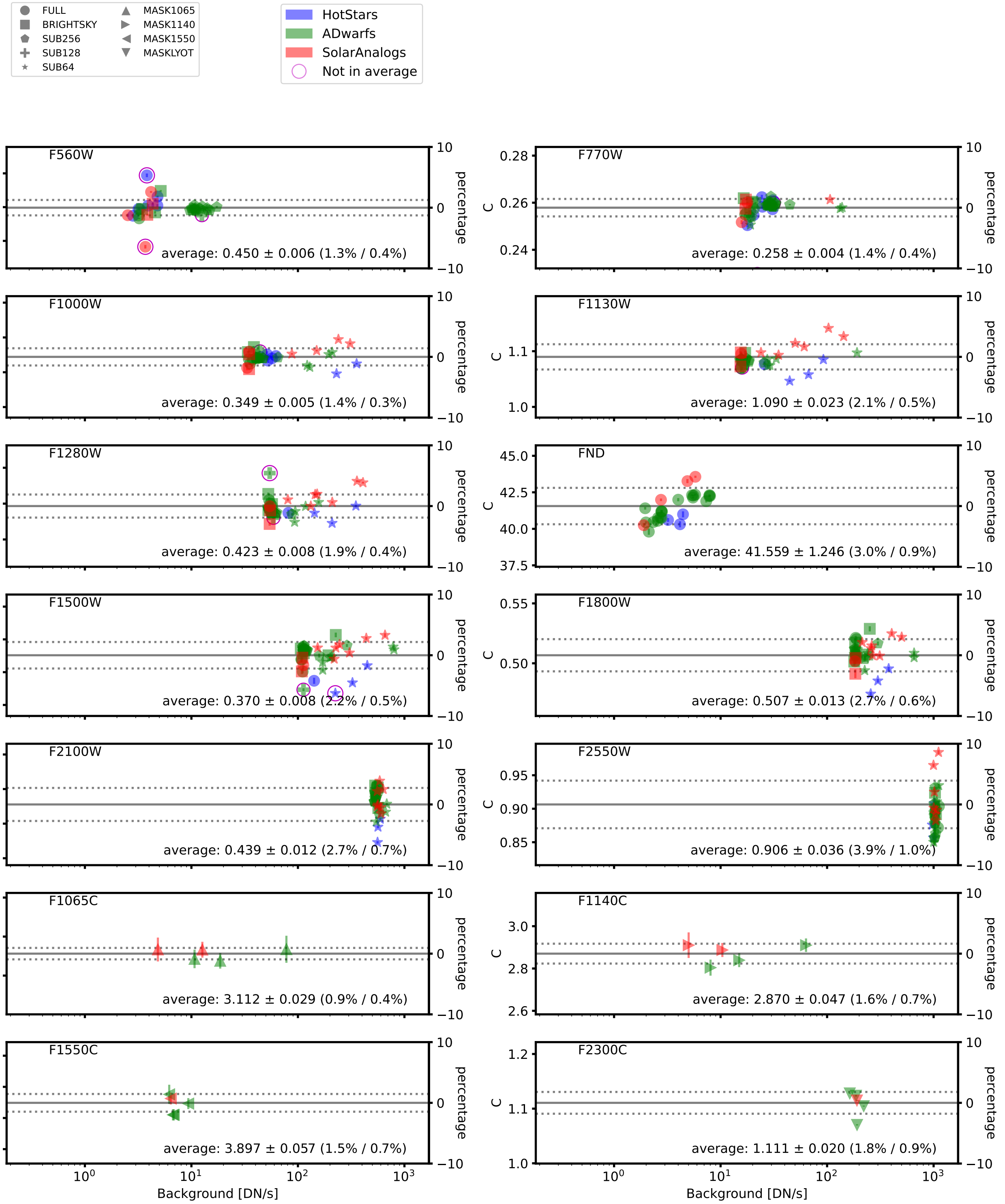

Figure 11. Same as Fig. 10 except plotted versus measured background.

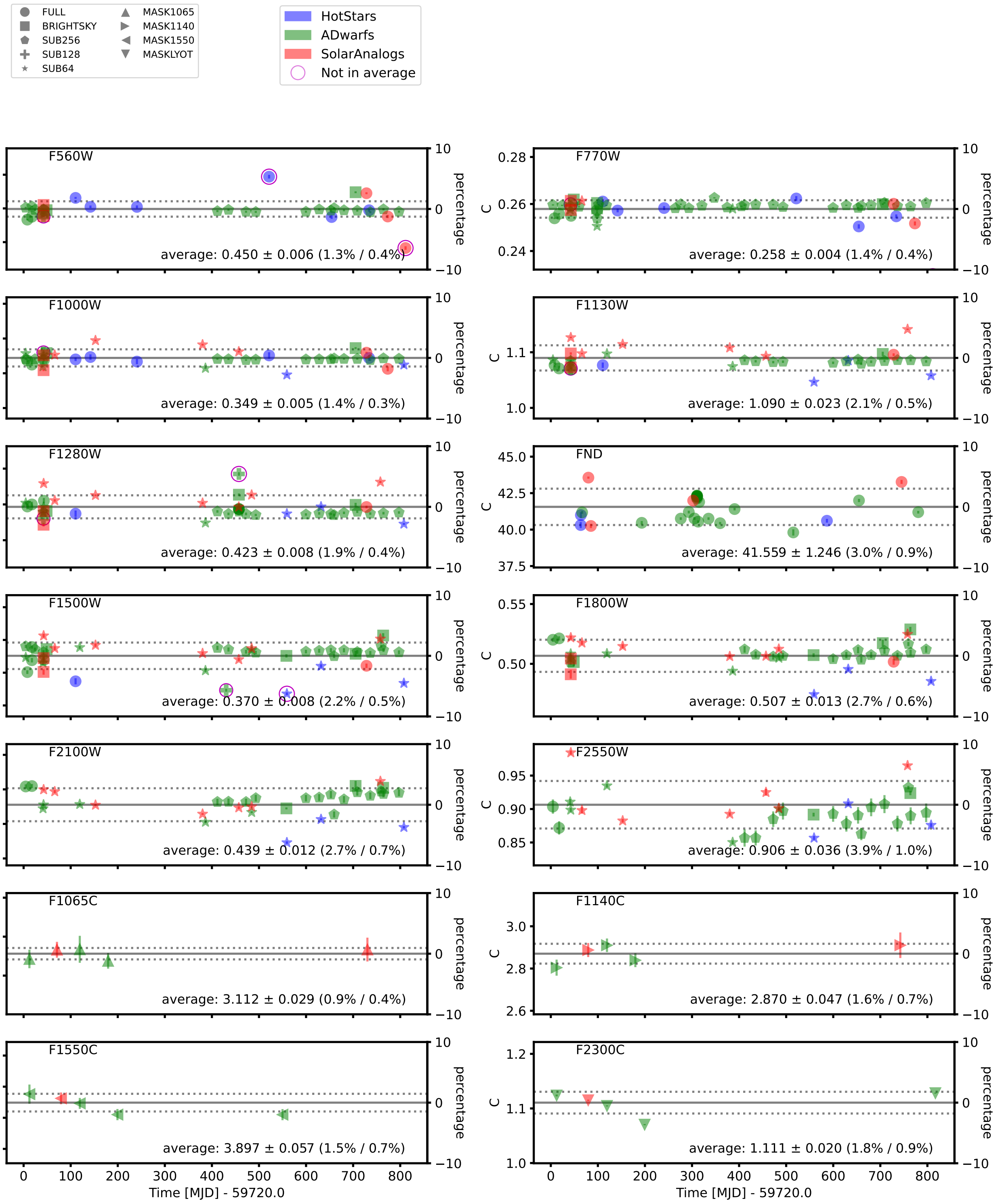

Figure 12. Same as Fig. 10 except plotted versus observation time.

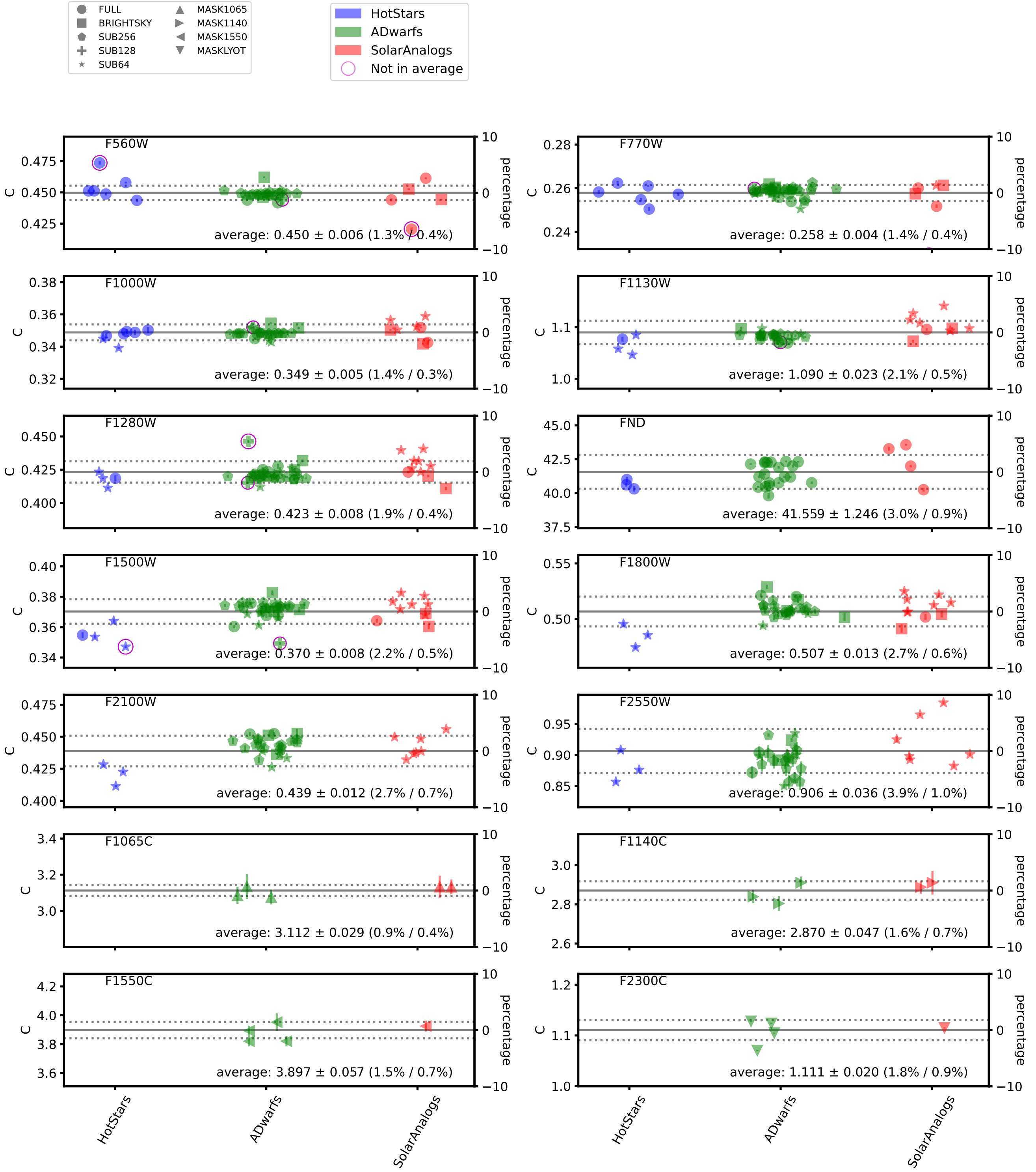

Figure 13. Same as Fig. 10 except plotted versus source type.

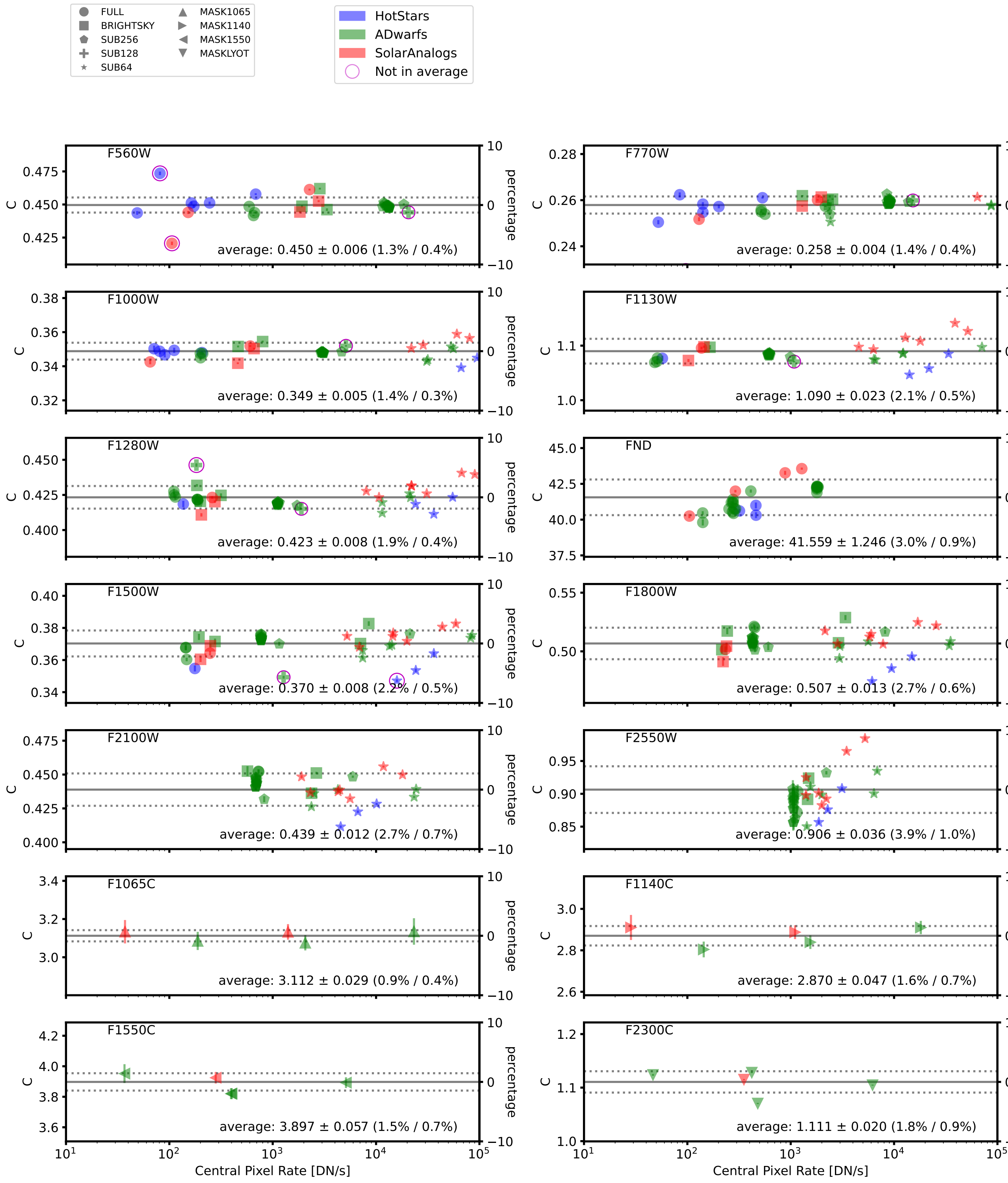

Figure 14. Same as Fig. 10 except plotted versus central pixel rate.

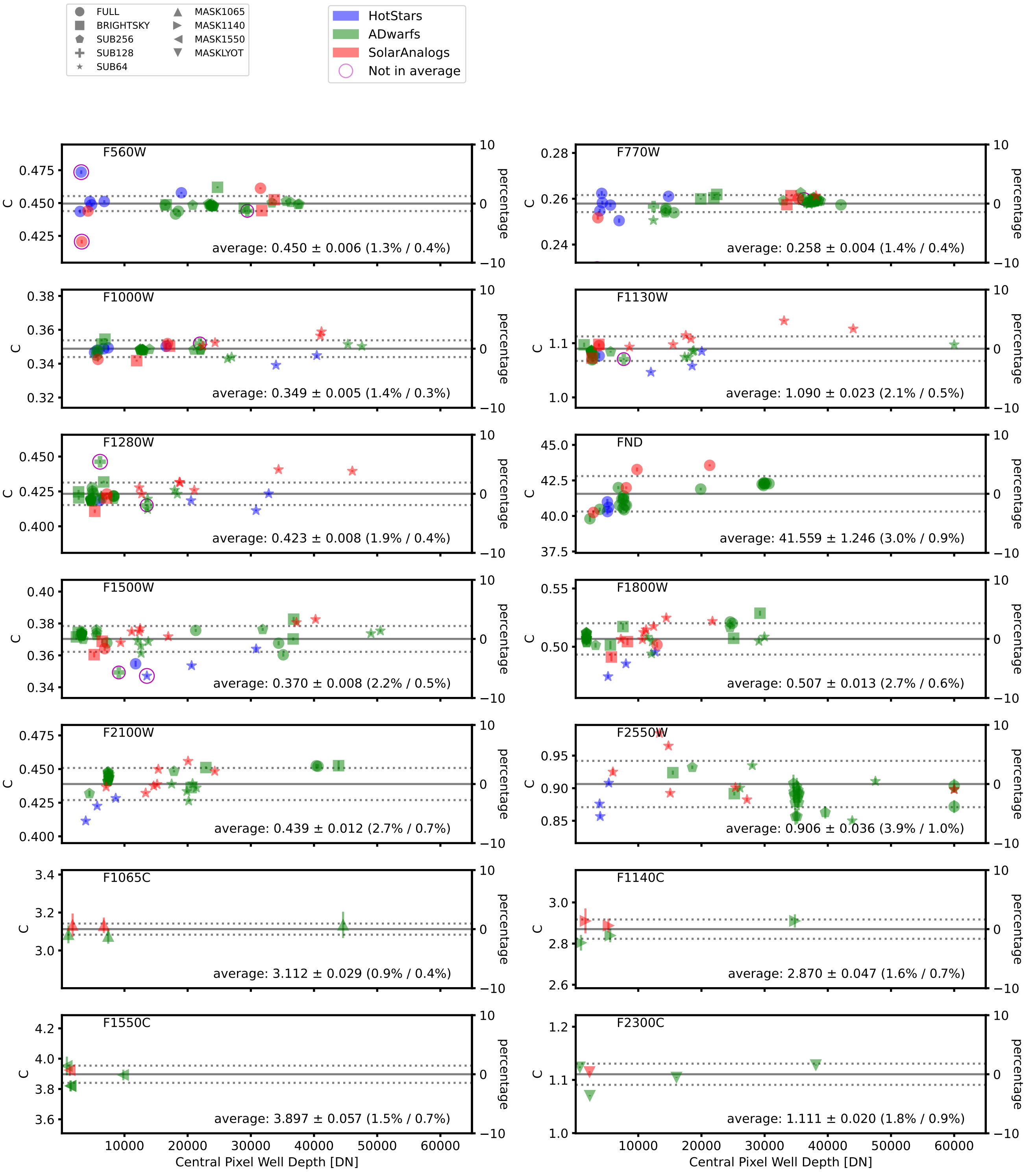

Figure 15. Same as Fig. 10 except plotted versus central pixel well depth.

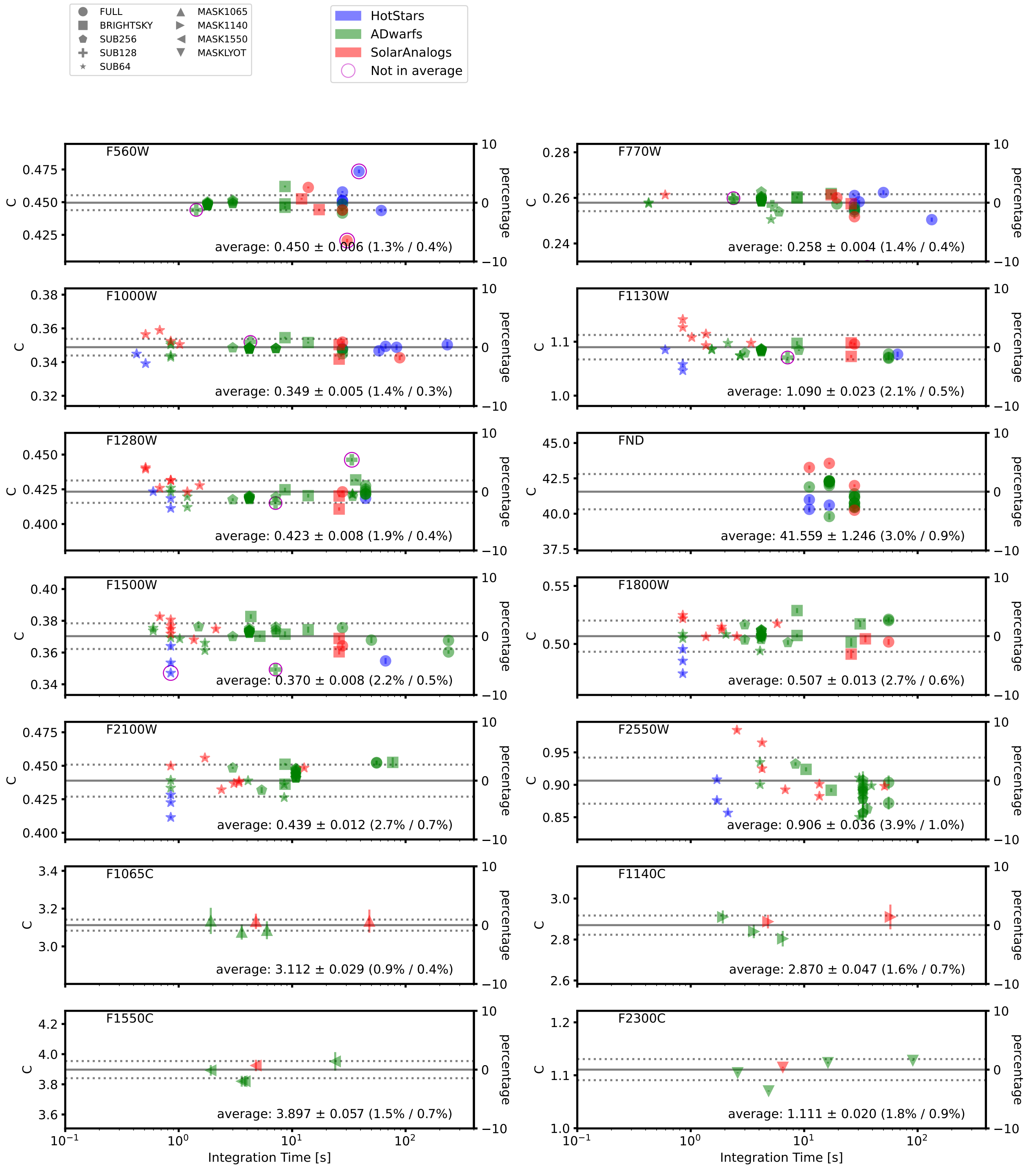

Figure 16. Same as Fig. 10 except plotted versus integration time.

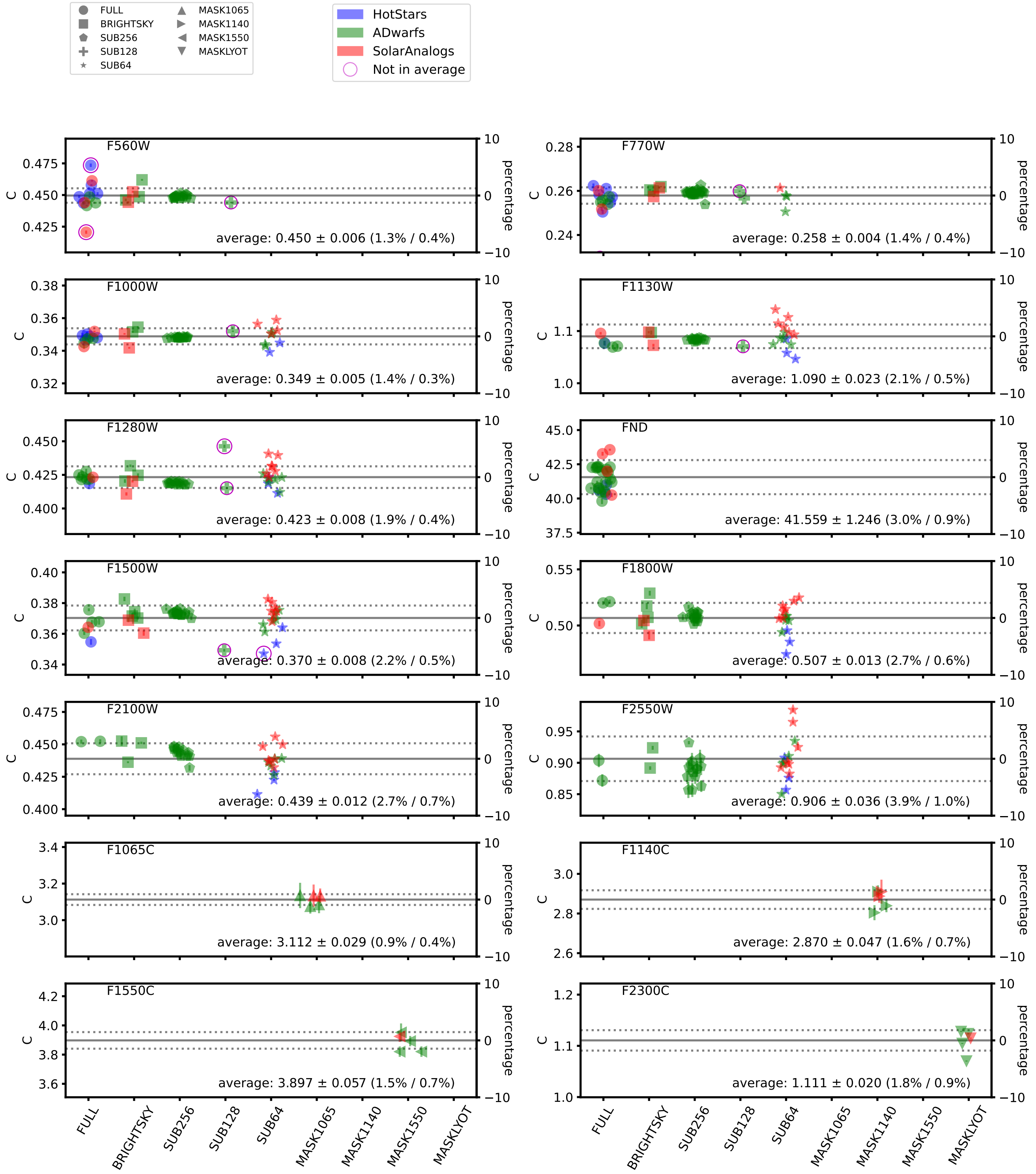

Figure 17. Same as Fig. 10 except plotted versus subarray.